LARGE BANDGAP QUANTUM SPIN HALL INSULATOR IN METHYL DECORATED PLUMBENE MONOLAYERS

A thesis submitted to the

Department of Electrical and Electronic Engineering (EEE)

of

Bangladesh University of Engineering and Technology (BUET)

In partial fulfillment of the requirement for the degree of

MASTER OF SCIENCE IN ELECTRICAL AND ELECTRONIC ENGINEERING

by

Shoaib Mahmud

(Roll No: 1017062225 F)

DEPARTMENT OF ELECTRICAL AND ELECTRONIC ENGINEERING (EEE)

BANGLADESH UNIVERSITY OF ENGINEERING AND TECHNOLOGY (BUET)

September 2020

The thesis titled **"Large Bandgap Quantum Spin Hall Insulator in Methyl Decorated Plumbene Monolayers"** submitted by Shoaib Mahmud, Roll No: 1017062225 F, Session: October 2017, has been accepted as satisfactory in partial fulfillment of the requirement for the degree of MASTER OF SCIENCE IN ELECTRICAL AND ELECTRONIC ENGINEERING on September 07, 2020.

Board of Examiners

1.	**Dr. Md. Kawsar Alam** Professor Department of EEE, BUET, Dhaka	Chairman (Supervisor)
2.	**Dr. Md. Kamrul Hasan** Professor and Head Department of EEE, BUET, Dhaka	Member (Ex-Officio)
3.	**Dr. Samia Subrina** Professor Department of EEE, BUET, Dhaka	Member
4.	**Dr. Mohammed Abdul Basith** Professor Department of Physics, BUET, Dhaka	Member (External)

Declaration

It is hereby declared that this thesis or any part of it has not been submitted elsewhere for the award of any degree or diploma.

Signature of the Candidate

shoaib mahmud

Shoaib Mahmud
(Student No: 1017062225 F)

Acknowledgement

At first, I express my solemn gratitude to Almighty Allah for giving me the patience and endurance to accomplish my M.Sc. thesis.

I would like to express gratefulness heartily to my thesis supervisor, Dr. Md. Kawsar Alam, Professor of Department of Electrical and Electronic Engineering (EEE), Bangladesh University of Engineering and Technology (BUET), for his cordial help, cogent suggestion and guidance throughout my thesis work. His academic research works have ushered before me the path of research to materials. I feel thankful to him for giving me enough freedom and complying with my capabilities, which made the research work very much pleasant for me. Throughout my life, I will be benefitted from the experience and knowledge that I have gained working with him.

I would like to thank the members of the board of examiners, Dr. Md. Kamrul Hasan, Dr. Samia Subrina and Dr. Mohammed Abdul Basith for taking the time to evaluate my work and provide me their valuable suggestions. Their suggestions will greatly help me to make my future research a more perfect one.

Abstract

Topologically protected edge states of quantum spin Hall (QSH) insulators have paved the way for dissipationless transport. In this regard, one of the key challenges is to find suitable QSH insulators with large bandgaps. Group IV analogues of graphene such as silicene, germanene, stanene, plumbene etc. are promising materials for QSH insulators due to their high spin-orbit coupling (SOC). Large bandgap opening may be possible in these group IV graphene analogues by chemical decoration. However, finding suitable chemical groups for such decoration has always been a demanding task. In this work, we investigate the performance of plumbene monolayer with $–CX_3$ (X=H, F, Cl) chemical decoration and report very large bandgaps in the range of 0.8414 eV to 0.9818 eV with spin-orbit coupling, which is much higher compared to most other topological insulators and realizable at room temperature. The thermodynamic and electronic stabilities are calculated from phonon dispersion curve and quantum molecular dynamics simulation. The $\mathbb{Z}_2$ topological invariants of the samples are calculated to confirm their topologically nontrivial property. The existence of edge states and topological nontrivial property are illustrated by investigating $PbCX_3$ nanoribbons with zigzag edges. Lastly, the change of structural and electronic properties of the topological materials with strain are demonstrated to extend the scope of using these materials. Our findings suggest that these derivatives are promising materials for spintronic and future high performance nanoelectronic devices.

Table of Content

Declaration ii

Acknowledgement iii

Abstract iv

Table of Content v

List of Figures vii

List of Tables xi

Chapter 1 Introduction xi

1.1 History and Background of Quantum Spin Hall Insulator 1

1.2 Literature Review 4

1.2.1 2D Quantum Spin Hall Insulators *4*

1.2.2 Group IV 2D Quantum Spin Hall Insulators *5*

1.2.3 Methods to Modify Spin-Orbit Coupling *6*

1.2.4 Cause of Using Methyl Decoration *6*

1.3 Role of Quantum Spin Hall Insulators in Magnetic Circuits 7

1.3.1 Generation of Spin Current *7*

1.3.2 Generation of Spin-Orbit Torque *9*

1.4 Objective of the Thesis 11

1.5 Overview of the Thesis 11

Chapter 2 Theory and Simulation Method 12

2.1 Methodology and Modeling 13

2.1.1 Density Functional Theory Calculation *13*

2.1.2 Parameters and Methodology Used *17*

2.1.3 Plumbene Monolayer Structure *19*

2.1.4 Methyl Decorated Plumbene Monolayer *20*

2.2 Determination of Electronic and Thermodynamic Stability 21

2.2.1 Calculation of Formation Energy *21*

2.2.2 Phonon Dispersion Curve *22*

2.2.3 Molecular Dynamics Simulation *22*

2.3 Quantum Spin Hall Insulators 23

2.3.1 Spin-Orbit Coupling and Bandgap Opening *23*

2.3.2 Spin Hall Effect *25*

2.3.3 Time-Reversal Symmetry *27*

2.3.4 Z_2 Topological Invariant *28*
2.4 Determination of Topological Nontriviality 29
2.5 Formation of Nanoribbon 31
2.6 Application of Strain 32
Chapter 3 Results and Topological Properties 33
3.1 Optimized Cells and Crystal Parameters 34
3.1.1 Optimized cells *34*
3.1.2 Crystal parameters *35*
3.2 Determination of Electronic and Thermodynamic Stability 36
3.2.1 Phonon Dispersion Curve *36*
3.2.2 Molecular Dynamics Simulation *37*
3.3 Bandstructures and Partial density of states 39
3.3.1 Bandstructure *39*
3.3.2 Verification of Bandgap with Hybrid Functional *41*
3.3.3 Partial Density of States *42*
3.4 Topological Invariant and Orbital Analysis 43
3.4.1 Topological Invariant *43*
3.4.2 Orbital Analysis *44*
3.5 Analysis of Nanoribbon 46
3.5.1 Determination of Topological Invariant *47*
3.5.2 Determination of Fermi velocity *48*
3.6 Change of Properties with Strain 48
3.6.1 Stability and Change of Bandgap *48*
3.6.2 Change of Bond Length *50*
Chapter 4 Conclusion and Future Works 51
4.1 Conclusion 52
4.2 Future Works 52

List of Figures

Figure 1.1 (a) In CdTe/HgTe/CdTe heterostructure, the normal structure when the thickness of HgTe layer is below 7nm, (b) inverted structure when the thickness of HgTe layer is more than 7nm, (c) there is no existence of edge states in normal structure, (d) the demonstration of symmetry-protected edge states in inverted structure. 3

Figure 1.2 (a) The spins are polarized in different directions in normal current flow, (b) So the net flow of spin is zero, (c) the edges states in quantum spin Hall insulator, (d) the net flow of spin. 8

Figure 1.3 The movement of domain wall in an easy-axis magnet due to the momentum exerted by spin current. The direction of the flow of spin from source determines the state of magnetization of the easy-axis magnet. 9

Figure 1.4 (a) Change of polarization states of magnetic domains by applying torque using topological insulators. The magnetic domains in magnetic materials are orienting themselves in the direction parallel to that of edge spins of topological insulators, (b) Change of polarization states due to the change of the spin current. 10

Figure 2.1 (a) A monolayer nanosheet of plumbene after cleaving bulk crystalline plumbene cell. (b) Side view of the nanosheet showing buckling height (δ) and Pb−Pb bond distance (d_1). 19

Figure 2.2 (a) Methyl decorated plumbene monolayer (top view) showing the unit cell with hexagonal crystal lattice, (b) Brillouin zone of the hexagonal crystal lattice with high symmetry points G, M, K, and (c) Side view of methyl decorated plumbene monolayer showing the Pb−Pb bond length (d_1), Pb−CX_3 bond length (d_2), buckling height (δ). 20

Figure 2.3 The methyl groups become attached to lead atoms of plumbene monolayer to form methyl decorated plumbene monolayer. The total energy of the methyl decorated plumbene monolayer should be less than the total energy of plumbene monolayer and isolated methyl groups to make the structure electronically stable. 21

Figure 2.4 Initial frame for molecular dynamics simulation of $PbCH_3$ monolayer. The CH_3 groups are released to become attached to lead atom sites. 23

Figure 2.5 (a) An electron circles an atomic nucleus, as viewed from the frame of reference of the nucleus, from the electron's frame of reference, the nucleus is circling it. The magnetic field experienced by the electron as a result, is directed upward from the plane of the path of motion. The interaction between the electron's spin magnetic moment and this magnetic field leads to the phenomenon of spin-orbit coupling, (b) Energy level splitting of an orbital due to spin-orbit coupling..... 24

Figure 2.6 (a) The deposition of charges on two opposite sides perpendicular to both magnetic field and direction of motion of charge is due to Hall effect, (b) The increase of magnetic field leads to quantized conductance leading to quantum Hall effect, (c) The circling of electrons with up and down spins in two opposite directions leads to two edge states which is called quantum spin Hall effect..... 25

Figure 2.7 (a) The change of Hall resistance and Longitudinal magneto-resistance with change of magnetic field. The hall resistance increases linearly with magnetic field at first, but with increase of magnetic field it becomes quantized. (b) The longitudinal magneto-resistance remains constant irrespective of applied magnetic field at first, but at high magnetic field it becomes zero with some spikes at the time of transient..... 26

Figure 2.8 Topologically protected edge states due to time-reversal symmetry which determines the direction of motion of electron from its spin. If an electron wants to change its direction of motion, then it will have to change its spin, as spin uniquely determine the direction of motion.27

Figure 2.9 (a) Edge states in quantum spin Hall insulators showing the spin of electrons, (b) Surface states in 3D topological insulators with spin of electrons. 29

Figure 2.10 Crystal unit cell of methyl decorated plumbene monolayer ($PbCX_3$) showing inversion symmetry. Each atom has its image about the point of inversion symmetry. 29

Figure 2.11 (a) $PbCH_3$ nanoribbon along zigzag direction. The dangling bond at the edge are passivated by hydrogen. (b) Top-view of the nanoribbon. 31

Figure 2.12 The method of applying strain to monolayer crystal cell. (a) Crystal cell after application of compressive strain, (b) Crystal cell after application of tensile strain..... 32

Figure 3.1 Crystal unit cell of methyl decorated plumbene monolayer ($PbCH_3$) after geometry optimization. The unit cell contains two lead atoms and two methyl groups. 34

Figure 3.2 Phonon dispersion curves showing no branch in the negative frequency region and thermodynamic stability at room temperature. (a) $PbCH_3$ monolayer, (b) $PbCF_3$ monolayer and (c) $PbCCl_3$ monolayer. 36

Figure 3.3 (a) The initial step (time = 0 ps) of molecular dynamics simulation of a $PbCH_3$ nanoribbon. It is periodic perpendicular to the page. (b) The stage of molecular simulation where CH_3 particles attain maximum kinetic energy (time = 0.054 ps), (c) The stable structure with no broken bond at room temperature (time=0.454 ps) and (d) Variation of system energy and temperature with respect to time. Red points, labelled as 1, 2 and 3, on the kinetic energy curve correspond to the position of the frames shown in (a), (b) and (c), respectively. 38

Figure 3.4 (a) The energy curve for molecular dynamics simulation of $PbCF_3$ nanoribbon. The curve shows the gradual stable state of the nanoribbon, (b) The final stable nanoribbon showing no breaking of bond at room temperature, (c) the energy curve for MD simulation of $PbCCl_3$ nanoribbon, (d) The final stable nanoribbon of $PbCCl_3$ showing no breaking of bond at room temperature. 39

Figure 3.5 (a) Bandstructure of the $PbCH_3$ monolayer showing the contribution of Pb $p_{x,y}$ and Pb p_z orbitals in forming the bands without spin-orbit coupling, (b) Bandstructure of the $PbCH_3$ monolayer with spin-orbit coupling. 40

Figure 3.6 (a) Bandstructure of $PbCF_3$ monolayer without and with spin-orbit coupling, (b) Bandstructure of $PbCCl_3$ monolayer without and with spin-orbit coupling. 40

Figure 3.7 Bandstructures without and with spin-orbit coupling employing HSE06 functional. (a) $PbCH_3$ monolayer (b) $PbCF_3$ monolayer. 41

Figure 3.8 (a) Partial density of states showing the contributions of Pb s, Pb $p_{x,y}$ and Pb p_z orbitals without spin-orbit coupling in $PbCH_3$ (b) Partial density of states with spin-orbit coupling. From the figures, it is seen that the major contribution to the bands near to Fermi level is due to Pb $p_{x,y}$ orbitals. (c) Partial density of states without spin-orbit coupling in $PbCF_3$, (d) Partial density of states with spin-orbit coupling in $PbCF_3$. 43

Figure 3.9 The orbital analysis of $PbCH_3$ at G(0,0) point, which shows that contribution of s and $p_{x,y}$ atomic orbitals to bands near Fermi level. The bandstructure formation is mainly due to crystal field splitting and spin-orbit coupling. 45

Figure 3.10 (a) $PbCH_3$ nanoribbon along zigzag direction. The dangling bonds at the edges are passivated by hydrogen. The blue and red colors arrows represent the edge states due to up and down spin respectively. (b) Bandstructure of zigzag $PbCH_3$ nanoribbon showing odd number of band passing through Fermi level which proves the Z_2 topological invariant of 1. The red color band corresponds to the bands due to edge states. (c) Bandstructure of zigzag $PbCF_3$ nanoribbon. (d) Bandstructure of zigzag $PbCCl_3$ nanoribbon. 47

Figure 3.11 (a) The change of bandgap (E_g) taking the effect of spin-orbit coupling (SOC) with change of strain, (b) the change of formation energy ΔE with strain. The negative values of formation energies ensure electronic stability. (c) The orbital analysis of $PbCH_3$ at G(0,0) point for different percentages of strain, which shows that contribution of s and $p_{x,y}$ atomic orbitals to bands near Fermi level. The amount of splitting in p-p orbitals is changed as shown by the dotted lines. 49

Figure 3.12 Change of buckling height (δ) and Pb−Pb (d_1) bond distance in $PbCH_3$ crystal cell with application of tensile and compressive strain. There is almost no change shown in the Pb−CH_3 atoms. 50

List of Tables

Table. 2-1 Parameters and their values used in structural and electronic calculation of Pb and $PbCX_3$ monolayer crystal cells. 18

Table. 3-1 Crystal lattice parameters (a) Pb−Pb bond length (d_1), Pb−CX_3 bond length (d_2), buckling height (δ_1), Energy bandgap with spin-orbit coupling (E_g), the formation energy (ΔE) and Z_2 topological invariant for different $PbCX_3$ monolayers. 35

Table. 3-2 Parities of 11 occupied spin-degenerated bands and symmetry functions at each symmetry points. The even and odd parities are represented by + and − signs. 44

Table. 3-3 Change of different types of bond lengths with the change of strain 51

Chapter 1

Chapter 1

Introduction

Topological insulators are new states of matter having a bulk bandgap like ordinary insulators and unique protected edge states which allow dissipationless transport [1, 2]. The edge states of topological insulators are protected by time-reversal symmetry which safeguards it from backscattering in presence of non-magnetic impurity [3]. Two-dimensional (2D) topological insulators are particularly fascinating due to their linear dispersion of energy band near Fermi level, leading to high Fermi velocity and mobility [4]. Topological insulators in the form of 2D materials, are called quantum spin Hall insulator, because of their similar properties to quantum Hall effect including spin degree of freedom.

1.1 History and Background of Quantum Spin Hall Insulator

The new topologically distinct electronic phase named the integer quantum Hall (QH) phase was discovered in 1980 AD [5]. It was shown in the discovery that Quantum Hall conductance can only take the values of integer multiple of $\frac{e^2}{h}$. The idea of such electronic phase was also considered for spin degree of freedom, where there were two QH phases with opposite spins [6]. The spin-orbit coupling took the role of magnetic field in these types of electronic phases. These type of 2D materials with topological insulating property were named as Quantum Spin Hall Insulator. The notable properties of Quantum Spin Hall insulator is that, the edge states exist in absence of a magnetic field due to the presence of spin-orbit coupling, and time-reversal symmetry (TRS) protects the edge states against any type of non-magnetic backscattering.

The quantum spin Hall phenomenon was first described in graphene by Kane and Mele [6], after the first transport experiment in graphene was done by Novoselov et al. in 2004 AD [7] and subsequently quantum Hall effect of graphene was measured in 2005 AD [8]. To propose the existence of a QSH state, Kane and Mele followed an earlier model for graphene introduced by F.D.M. Haldane, where periodic magnetic field with no net flux led to a quantized Hall (QH) effect [9]. The Kane – Mele model indeed described two copies of the (spin-less) Haldane model such that spin-up electrons exhibit an anti-chiral integer QH effect and spin-down electrons show the chiral QH effect. The QSH effect shows a quantized spin-Hall conductance and a vanishing charge-Hall conductance.

Though graphene was first proposed to be quantum spin Hall insulator theoretically but, HgTe/CdTe [10] and InAs/GaSb [11] heterostructures have been first experimentally proven to be 2D topological insulators. A model of topological insulators was proposed by Bernevig, Hughes and Zhang (BHZ), easily achievable in experiment, in which a thin mercury telluride (HgTe) sheet of about 7nm is sandwiched between two sheets of cadmium telluride (CdTe) thus forming a quantum well of CdTe/HgTe/CdTe heterostructure as shown in **Figure 1.1** (b). The known inverted band structure in HgTe combined with confinement to open a gap in it, resulted in the prediction of edge channels with quantized conductance, which were subsequently identified by the group of L.W. Molenkamp [12]. Here the transition from normal structure to inverted structure [**Figure 1.1** (a) and (b)] leads to band inversion which is the cause of formation of edges states [**Figure 1.1** (c) and (d)].

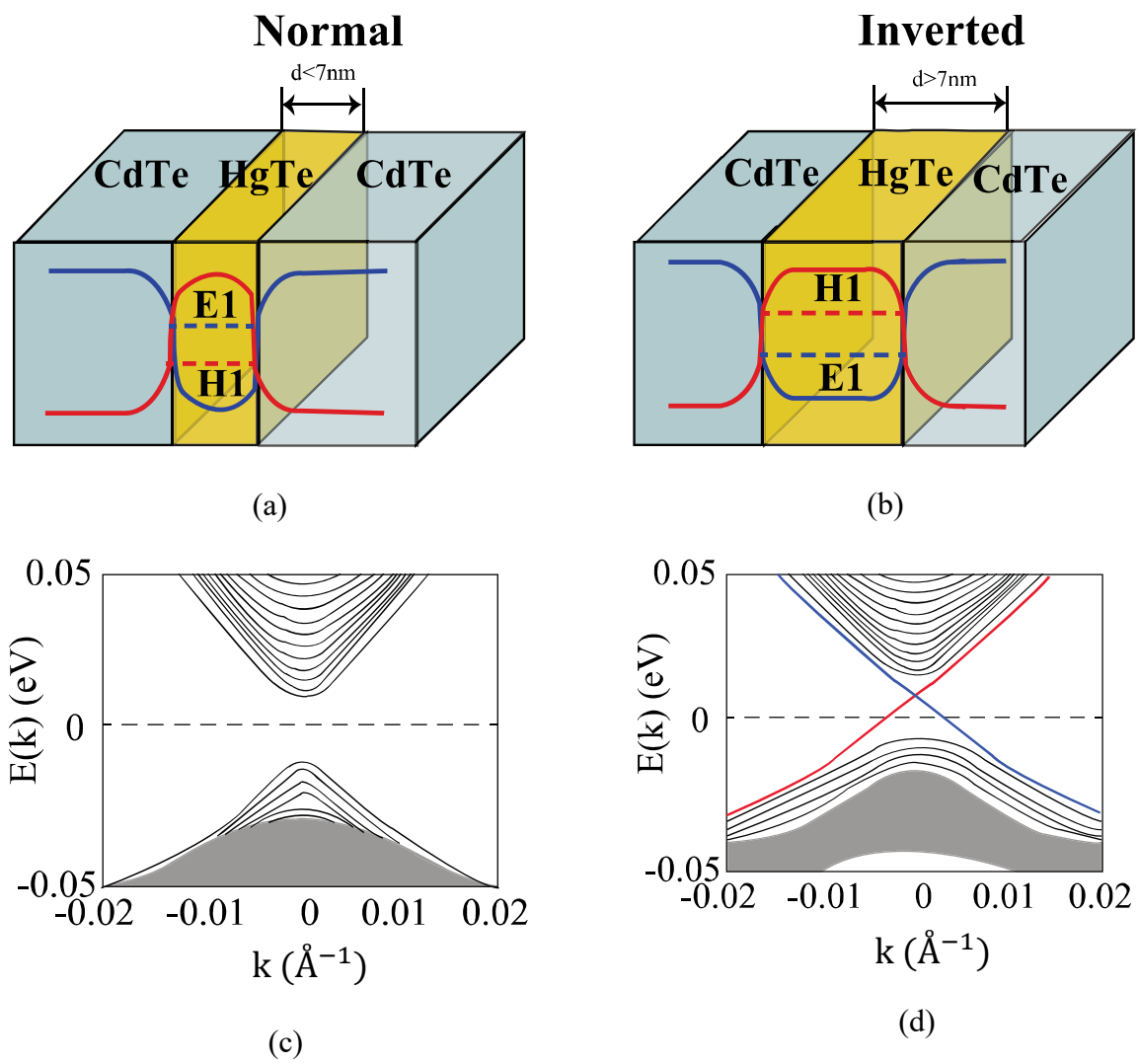

Figure 1.1 (a) In CdTe/HgTe/CdTe heterostructure, the normal structure when the thickness of HgTe layer is below 7nm, (b) inverted structure when the thickness of HgTe layer is more than 7nm, (c) there is no existence of edge states in normal structure, (d) the demonstration of symmetry-protected edge states in inverted structure.

After the experimental observation of the QSH effect in inverted HgTe QWs, it has been predicted that this effect occurs also in type-II semiconductor QWs made from InAs/GaSb/AlSb heterostructure in the inverted regime. In this QW structure, as in the HgTe/CdTe system, the QSH state can be observed when the Fermi level lies inside the gap. However, the bandgaps are so small

that topological edge states can only be found below 10 K. Also the buried edge states in these heterostructures, make it difficult to probe these states. But these experiments sparkled excitement and encouraged further experiment on topological insulators.

1.2 Literature Review

1.2.1 2D Quantum Spin Hall Insulators

Research into quantum spin Hall insulating properties of 2D materials, has become an interesting topic after the invention of quantum spin Hall insulator. Among the mentioned 2D materials system, the remarkable ones are transition metal dichalcogenides (TMDC), group II-VI, III-V and IV hexagonal buckled graphene-analogues. A number of first-principles based research have been conducted on these types of materials system.

Two-dimensional transition metal dichalcogenides, MX_2 (M=Mo, W and X=S, Se, Te) shows topological electronic properties by external electric field [13]. Transition-metal halide MX (M = Zr, Hf; X = Cl, Br, and I) monolayers have also been predicted as a novel family of two-dimensional QSH insulators [14]. MoS_2, WTe_2 and WSe_2 have been demonstrated to show quantum spin Hall insulating properties [15-18].

Group IV, III, III-V, IV-VI graphene-analogues are particularly drawing attention due their similar properties to graphene. Among the group III elements phosphorene [19], Antimonene [20, 21], Arsenene [22-24], Bismuthene [25] have shown quantum spin Hall insulating properties. The group IV elements that have shown quantum spin Hall insulating properties are silicene, germanene and stanene. The remarkable III-V elements are GaBi [26], TlA (A=N, P, As, and Sb) [27, 28], III-Bi based two-dimensional materials [29] and InSb 2D compound [30]. Thus

hexagonal graphene-analogues of group III, IV, V and VI elements are keeping major role in the field of 2D topological insulators.

Though most of these are based on first-principles simulation, but development in fabrication technology is paving the way for experimental realization of quantum spin Hall insulating properties of these types of materials system.

1.2.2 Group IV 2D Quantum Spin Hall Insulators

In spite of having outstanding electrical, thermal, and mechanical properties, as well as very long spin diffusion lengths at high-temperature in graphene, its band gap is still very small (10^{-3} meV) [31]. 2D materials having honeycomb structure like graphene, have shown to possess remarkable spin-orbit coupling and linear dispersion of energy near Fermi level [32-35]. The larger spin-orbit coupling leads to higher bandgap in the bulk and linear dispersion of energy causes high Fermi velocity of electron, which makes such materials suitable for high-speed device application. Group IV analogues of graphene (silicene, germanene, stanene, plumbene) with notable spin-orbit coupling, have recently drawn noteworthy attention due to the presence of Dirac fermion in them, similar to graphene [32, 36-40]. Nonetheless, reported bandgap opening due to spin-orbit coupling in silicene (1.55 meV) [41], germanene (23.9 meV) [41], stanene (73.5 meV) [42] are not sufficient for room temperature operation. On the other hand, monolayer plumbene has drawn attention in recent time particularly due to its large bandgap opening at room temperature [43, 44]. Since, plumbene does not show topological nontrivial characteristics normally [38, 43], we need additional transformation technique of chemical decoration to have topological nontrivial characteristics in it and take the advantage of this large spin-orbit coupling.

1.2.3 Methods to Modify Spin-Orbit Coupling

The spin-orbit coupling can be engineered if we can modify the wavefunction of the electrons around nucleus. Chemical decoration [43, 45-48], application of electric field [49, 50], substrate engineering [51] and absorption or adsorption adatoms [52, 53] are among the few techniques that have been used for modification of spin-orbit coupling and topological properties in group IV monolayers. For the electric field method, the bandgap opening is sometimes too small to operate at room temperature and breakdown electric field of materials constraints the range of applied electric field [54]. Also, substrate engineering has the limitation of very small bandgap opening, and the interaction between materials and the substrate may damage the crystalline structure [43, 51]. Moreover, doping and molecular adsorption can distort the crystal structure leading to difficulty in fabrication and device integration [53]. Chemical decoration is the most appealing method among the mentioned techniques as it offers large bandgap opening while maintaining structural and electronic stability of the material. So, chemical decoration in graphene analogues of 2D materials, has become a matter of great interest in recent times, as they have been reported to offer the highest bulk bandgap for topological insulators [43-45].

1.2.4 Cause of Using Methyl Decoration

Finding a suitable group for chemical decoration to have topological property is the main challenging task. It has been proven theoretically that hydrogen and halogen decoration would provide large bandgap [36, 43, 55]. However, experimental works have been reported showing plasma hydrogenation and fluorination of materials rapidly increase defects and disorders [56, 57]. Therefore, alkyl and alkyl halide decoration of silicene, germanene, stanene and plumbene are suitable alternatives as such decoration may provide bandgap comparable to that of hydrogenation and halogenation without noticeably increasing the defects and disorders [46, 58, 59]. Methyl

derivatives among alkyl groups have shown preferable result in silicene, germanene, stanene and other 2D materials with hexagonal honeycomb structure similar to graphene [4, 60-62]. For example, methyl decorated silicene, germanene and stanene have shown quantum spin Hall effect at 25% [62], 12% [61] and 4% [4] strain, respectively. However, integrating them into devices using external strain is a very complex process. Quantum spin Hall effect in methyl decorated silicene, germenane and stanene suggest that it is worth exploring the behavior of methyl decorated plumbene ($PbCH_3$), that has remained unexplored, as of yet.

1.3 Role of Quantum Spin Hall Insulators in Magnetic Circuits

Quantum spin Hall insulators are being considered to be used in magnetic circuits, as they can apply high spin-orbit torque and produce pure spin current. The high spin-orbit torque can be used to alter the state of magnetization of the particular magnet. The spin current can shift the domain wall in magnets to change the direction of spin of electrons. So, quantum spin Hall insulators are encouraging the use of magnet in logic purpose.

1.3.1 Generation of Spin Current

Charge current is the net flow of charge per unit time through any cross-sectional area. Spin current is net flow of spin per unit time. In conventional current, the spins of electrons are oriented in different directions, so the net spin flow is zero as shown in **Figure 1.2** (a) and (b). So to produce net spin current, we will have to polarize these electrons in any particular direction. This can be done by filtering the charge current through any magnetic materials but as most of the magnetic materials are non-conducting so it is difficult to obtain this type of filter. But, it is possible to obtain pure spin current along the edge of quantum spin Hall insulators. Along the edge of quantum spin

Hall insulators, electrons with opposite spin flow in opposite directions (**Figure 1.2** (c)). So there is a net flow of spin along the edges resulting in a spin current as presented in **Figure 1.2** (d).

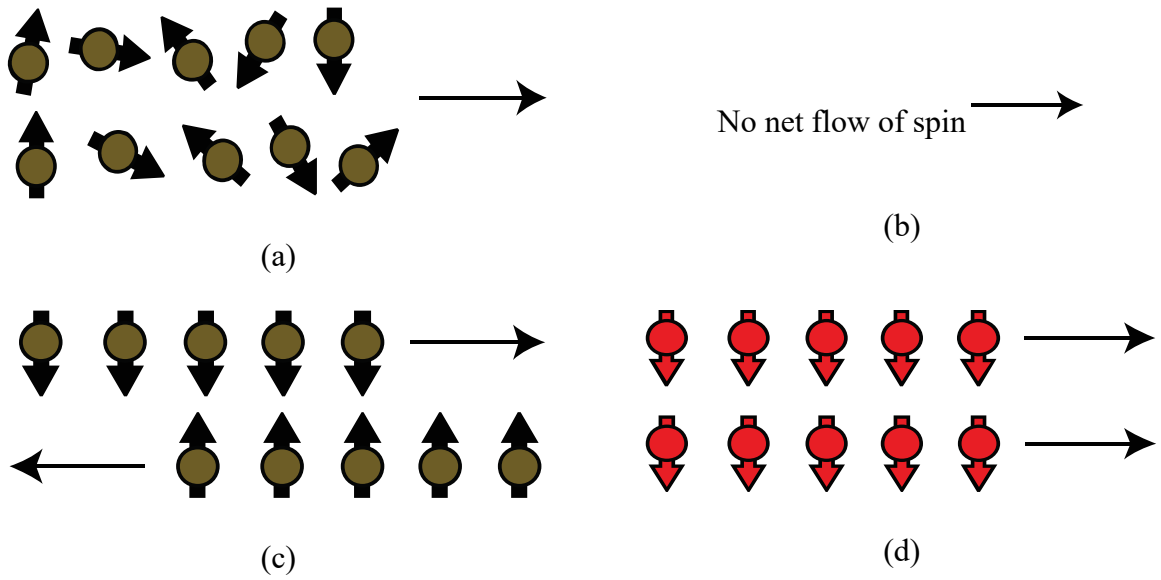

Figure 1.2 (a) The spins are polarized in different directions in normal current flow, (b) So the net flow of spin is zero, (c) the edges states in quantum spin Hall insulator, (d) the net flow of spin.

If topological insulator is magnetically doped then it is possible to obtain quantum anomalous Hall effect where only spin of one kind flows through the edge. The spin current in quantum anomalous Hall insulator can be used to move the domain wall in an easy-axis magnet as shown in **Figure 1.3**. Domain wall is the transition between different magnetic moments. Now, if spin current is flown from left source in **Figure 1.3** then it will apply a momentum to electrons in the magnetic material. So the magnetic domain wall will shift to the right [63, 64]. Thus, flowing of spin current from left to right, it is possible to change the polarization state of magnetic domain through the shift of the domain wall.

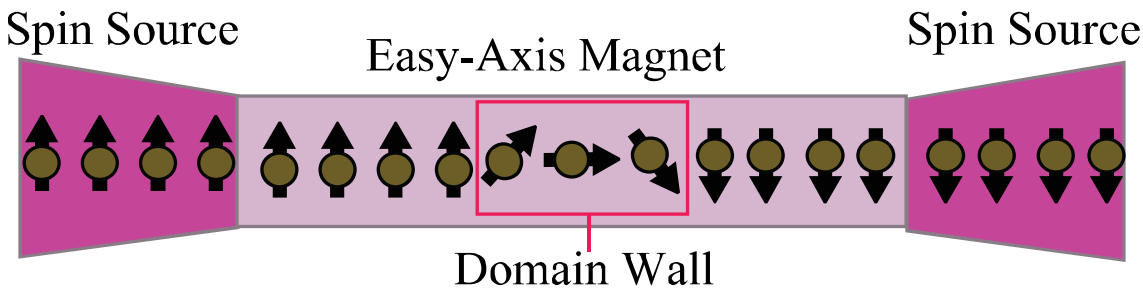

Figure 1.3 The movement of domain wall in an easy-axis magnet due to the momentum exerted by spin current. The direction of the flow of spin from source determines the state of magnetization of the easy-axis magnet.

1.3.2 Generation of Spin-Orbit Torque

Magnetic circuit is specially drawing attention due to its non-volatility and low power consumption [65-69]. The different states of magnets are used for different values in logic operation. To change the states of magnet, we will have to change the state of polarization of the magnet. This can only be obtained by applying high spin-orbit torque to the polarization state of the magnet. This can be achieved by creating an interface between topological insulator and magnetic materials. The use of topological insulators is particularly useful here, as the electrons in topological insulators can apply high spin-orbit torque (orbital momentum due to spin-orbit coupling is associated with spin angular momentum). So, the applied momentum due to spin here is more than $\frac{\hbar}{2}$ [70].

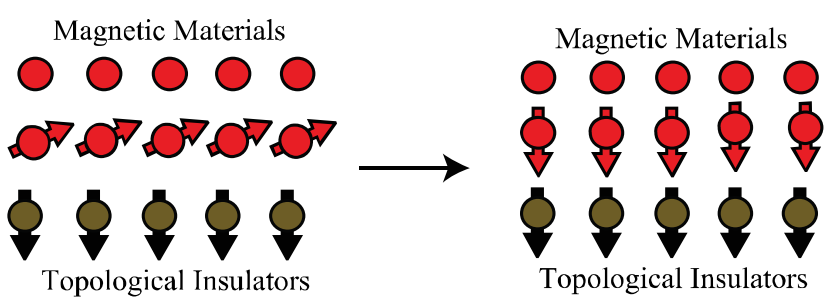

(a)

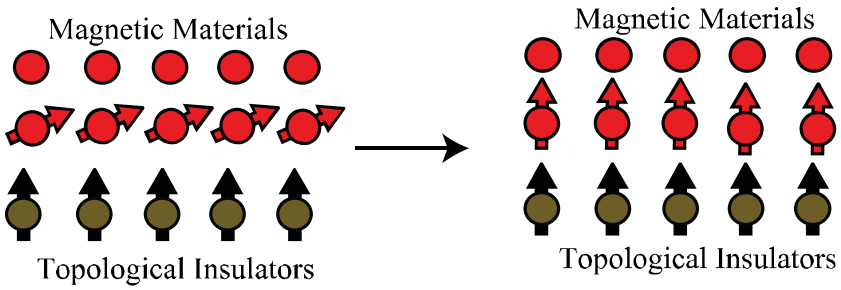

(b)

Figure 1.4 (a) Change of polarization states of magnetic domains by applying torque using topological insulators. The magnetic domains in magnetic materials are orienting themselves in the direction parallel to that of edge spins of topological insulators, (b) Change of polarization states due to the change of the spin current.

The change of polarization states of a magnet with the help of application of spin-orbit torque using topological insulators is shown in **Figure 1.4** [71]. The magnetic domain at interface of topological insulator and magnetic materials, is taking the direction of spin of the topological insulators, as the electron spin on topological materials is applying a net torque on the magnetic materials. Thus forming an interface of a magnetic materials with topological insulator, it is possible to alter the polarization direction of the magnetic domains of the magnetic material, depending on the direction of applied torque. There are many ways in which the magnets can be manipulated through topological insulators. Thus topological insulators will play a major role in future spintronic devices based on magnet.

1.4 Objective of the Thesis

The objectives of this work are:

1. To explore the electronic and thermodynamic stability of methyl and trihalogenomethyl decorated plumbene monolayers, and find the amount of bandgap opening due to spin-orbit coupling (SOC) in these materials.

2. To find out the $\mathbf{Z}_2$ topological invariant of these materials, and check whether they exhibit strong quantum spin Hall insulating property or not.

3. To investigate the existence of edge states in hydrogen-passivated nanoribbons of methyl and trihalogenomethyl decorated plumbene monolayers, and find out the topological nontriviality of the materials analyzing their bandstructures.

4. To observe the effect of strain on structural and electronic properties of these materials. As strain is one of parameters to engineer wavefunction of electron, so through the application of strain, it is possible to change the electronic properties.

1.5 Overview of the Thesis

Chapter 1 mentions the historical background of quantum spin Hall insulators and literature review of research on 2D quantum spin Hall insulators. The application of quantum spin Hall insulators in magnetic circuits are also shown followed by objective of the thesis.

Chapter 2 presents details about different structures of the materials system and the simulation methodology that has been used in this thesis. It also presents the idea of spin-orbit coupling, and how the phenomenon of quantum spin Hall effect is related to spin-orbit coupling. The parameters used for density functional theory (DFT) simulation are also discussed in this chapter.

Chapter 3 provides the results of structural and electronic simulation, and topological properties that are obtained in these materials. The cause of having those properties are briefly explained in this chapter, and different types of data and their values are justified.

Chapter 4 discusses the conclusion and the future scope of research on these types of materials system.

Chapter 2

Chapter 2

Theory and Simulation Method

2.1 Methodology and Modeling

Topologically insulating phases were proposed theoretically at first and after that these were observed experimentally. For theoretical proposition of these types of materials, numerical simulation of their electronic and structural properties is necessary.

The electronic and structural properties of novel materials can be found by numerical simulation in First-Principles simulation methods. As these methods are not based on any external parameters, so it is suitable for proposing novel materials. Density Functional Theory (DFT) simulation has become particularly popular among first-principles based simulations, because of its accuracy with experimental results and less computational cost [72, 73]. The first experimental works on Bismuth Chalcogenide (Bi_2X_3, X=Se, Te) TIs have been supported by DFT simulations [74]. Other properties of different topological materials obtained from DFT-based calculations, have been verified in experiments [75-77]. Thus DFT-based numerical simulations are keeping motivating to predict new topological materials.

Here, we have performed density functional theory (DFT) based first-principles calculations using Synopsys Quantumwise ATK simulation package [78]. QuantumATK is a complete atomistic simulation toolkit developed and supported by world leading atomic-scale modeling experts.

2.1.1 Density Functional Theory Calculation

The many-body properties in real materials system can be formulated in DFT, if exchange-correlation functional is known. The Hamiltonian of many-body Schrodinger equation of a

practical material system with interacting electrons and nuclei after Born-Oppenheimer approximation can be written as –

$$\hat{H} = -\sum_{i}\left[\frac{\hbar^2}{2m_e}\nabla_{r_i}^2 + V_{ext}(r_i)\right] + \frac{1}{2}\sum_{i\neq j}\frac{e^2}{|r_i - r_j|} + E_{II} \tag{2.1}$$

Where, $V_{ext}(r) = \sum_I \frac{Z_I e^2}{|r-R_I|}$ is the external potential due to the nuclei located at R_I,

E_{II} is the classical interaction of the nuclei with each other.

In Born-Oppenheimer approximation, the nuclei are considered as stationary due to its larger mass compared to electrons, so the kinetic energy term due to nuclei is omitted. It is difficult to obtain wavefunction of electron from Hamiltonian of Equation (2.1), when the number of electrons and nuclei is more, as it contains the coulomb interaction potential term between them. This problem can be solved if we can modify the Hamiltonian to a single particle Hamiltonian. This is done in Density Functional Theory simulation, based upon a proof by Hohenberg and Kohn (1964) [79] that many-body ground-state wavefunction can be expressed as a functional of ground-state electron density. The ground-state electron density can also be expressed as a functional of ground-state energy. Subsequently, Kohn and Sham (1965) [80] states that Hamiltonian of noninteracting electrons can be formulated keeping the ground-state electron density unchanged. The effective single particle Kohn-Sham Hamiltonian is –

$$\hat{H}_{KS} = -\frac{\hbar^2}{2m_e}\nabla_r^2 + V_{KS}^{[n]}(r) \tag{2.2}$$

Where, Kohn-Sham potential $V_{KS}^{[n]}(r)$ is functional of electron-density $n(r)$ and,

$$V_{KS}^{[n]}(r) = V_{ext}(r) + V_H^{[n]}(r) + V_{XC}^{[n]}(r) \tag{2.3}$$

where,

$$V_H^{[n]}(r) = e^2 \int \frac{n(r')}{|r - r'|} d^3r' \tag{2.4}$$

is the Hartree potential, modeling the electron repulsion potential.

$$V_{XC}^{[n]}(r) = \frac{\delta E_{XC}[n]}{\delta n(r)} \tag{2.5}$$

is the exchange-correlation potential, which encodes nonclassical many-body effects.

The eigensolution of the single particle Kohn-Sham Hamiltonian is –

$$\hat{H}_{KS}|\psi_i\rangle = E_i|\psi_i\rangle \tag{2.6}$$

The ground-state solution is constructed finding N lowest eigenvalues and the charge density is given by –

$$n(r) = \sum_{i=1}^{N} |\psi_i(r)|^2 \tag{2.7}$$

The charge density is then used in Equations (2.4) and (2.5) to re-construct the Hamiltonian $\hat{H}_{KS}$ and the process is iterated to obtain $n(r)$ and $V_{KS}^{[n]}(r)$.

In DFT, the exchange-correlation energy is approximated by different methods. In Local density approximation (LDA) [81], the exchange-correlation energy per electron of the interacting electron gas at point r is approximated by that of the homogeneous electron gas with the same density as the interacting electron gas. It is simplest approximation to exchange-correlation functional, E_{xc}. The Local density approximation of exchange correlation functional has the form –

$$E_{XC}^{[n]}(r) = \int n(r)\epsilon_{XC}\big(n(r)\big)\, d^3r \tag{2.8}$$

where $\varepsilon_{xc}^{hom}(n)$ is the exchange-correlation energy density of the homogeneous electron gas with density n. A wide range of properties for atoms, molecules and solids can be successfully described by the LDA, in spite of its simple local form.

As the LDA approximates the energy of the true density by the energy of a local constant density, it fails in situations where the density undergoes rapid changes such as in molecules. An improvement to this can be made by considering the gradient of the electron density, the so-called GGA [82]. The GGA improves on the LDA by using the gradient of electron density in addition to its value, and has the form –

$$E_{XC}^{[n]}(r) = \int n(r)\epsilon_{XC}\big(n(r)\big)\, F_{XC}(n, |\nabla n|) d^3r \tag{2.9}$$

where $\varepsilon_{xc}^{hom}(n)$ is the exchange-correlation energy density of the homogeneous electron gas with density n, and F_{xc} is dimensionless. The most popular functional for the GGA is the parameterization of Perdew-Burke-Ernzerhof (PBE).

Both LDA and GGA have been successfully employed to calculate and predict the topologically nontrivial properties in topological insulators in very good agreement with the experimental findings. However GGA-PBE functional is commonly used compared to functional in LDA method due to its more accuracy.

In order to assess more accurately the electronic band structure parameters such as the bandgap, a hybrid functional has been employed. Hybrid functional approximates exchange correlation energy functional in DFT by incorporating a portion of exact exchange from Hartree-Fock theory with the rest of the exchange-correlation energy from other sources. The exact exchange energy functional is expressed in terms of the Kohn-Sham orbitals rather than the density, so it is termed an implicit density functional. Exchange correlation, E_{xc} is approximated in HSE06 hybrid

functional by separation of electron interaction in the exchange energy into short-range and long-range part. This method generally gives more accurate bandstructure than that of GGA-PBE method but computationally expensive.

Also, to consider only the effect of valence electrons, different types of pseudopotential are considered as core electrons do not play much role in properties of materials and increase computational cost [83]. By pseudopotential, the attraction of electrons to nucleus, that is $V_{ext}(r_i)$ is modeled by an effective potential $V_I(|r - r_I|)$. To implement the DFT-code in software, different basis-sets such as plainwave basis-set or linear combination of atomic orbitals (LCAO) are considered. In case of plainwave basis-set, the wavefunctions of electrons are considered as plainwave. On the other hand, in case of LCAO, the electrons are localized as atomic orbitals.

2.1.2 Parameters and Methodology Used

The geometry of plumbene monolayer has been optimized using Limited-memory Broyden-Fletcher-Goldfarb-Shanno (LBFGS) optimization algorithm [84]. Structural relaxation is implemented until force on each atom becomes less than force tolerance and stress on crystal cell is less than stress error tolerance. In this regard, the linear combination of atomic orbitals (LCAO) calculator is used with generalized gradient approximation (GGA) – Perdew-Burke-Ernzerhof (PBE) exchange correlation method [85]. The self-consistent field (SCF) simulation is continued until it reaches the accuracy of iteration control tolerance. The Brillouin zone is sampled by using 9×9×1 Gamma centered Monkhorst Package [86]. The vacuum distance is set to 30Å which is sufficient to avoid interaction between two parallel layers. Spin-orbit coupling is included in the calculation using non-collinear spin-orbit interaction method [87] and SG15-SO pseudopotential [88]. The parameters and their values used in the simulations are given in **Table. 2-1**. To validate the parameters of our simulation method, we have recalculated the bandstructures of these

materials system with HSE06 hybrid-functional [89]. The use of HSE06 hybrid-functional gives more accurate results which can be compared with the results obtained using GGA-PBE functional.

Table. 2-1 Parameters and their values used in structural and electronic calculation of Pb and $PbCX_3$ monolayer crystal cells.

Parameter	Value
Force tolerance	0.01 eV/ Å
Stress error tolerance	0.001 eV/ $Å^3$
k-point sampling	9×9×1
Pseudopotential (SOC)	SG15-SO
Density mesh cut-off	125 Hartree
Iteration control tolerance	10^{-5} eV
Pseudopotential (without SOC)	PseudoDojo
Damping factor	0.1

Next, we have decorated the plumbene monolayer sheet with $–CX_3$ (X = H, F, Cl) groups and repeated the geometry optimization process using the same procedure. The bandstructure and partial density of states (PDOS) for each case of the decorated structures without and with spin-orbit coupling are calculated to find out the properties of the monolayers as well as orbital analysis of the materials.

2.1.3 Plumbene Monolayer Structure

The 2D materials can be built experimentally from their bulk structure by cleaving or exfoliation, or by their direct growth using different types of chemical vapor deposition (CVD) technology [90, 91]. Here, we have prepared a 2D plumbene nanosheet by cleaving the bulk crystalline plumbene cell, whose top view and side view along with crystal unit cell have been shown in **Figure 2.1**.

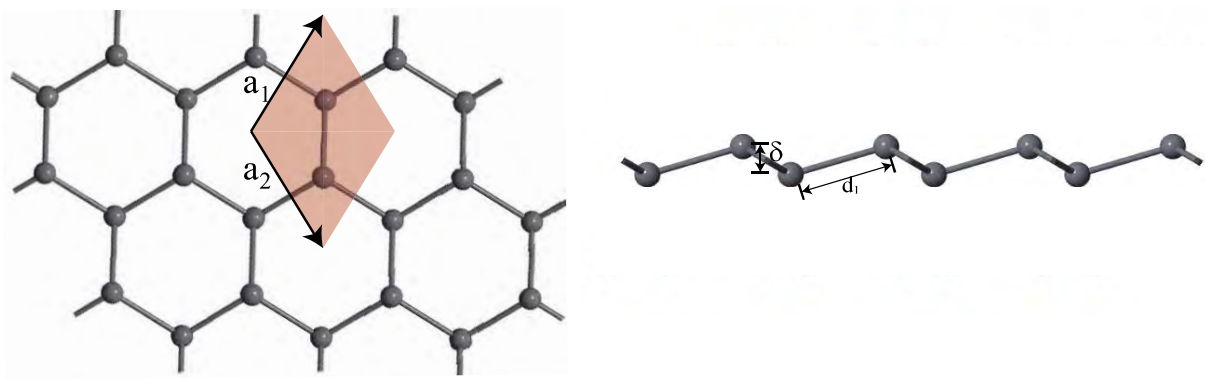

(a) (b)

Figure 2.1 (a) A monolayer nanosheet of plumbene after cleaving bulk crystalline plumbene cell. (b) Side view of the nanosheet showing buckling height (δ) and Pb−Pb bond distance (d_1).

It is evident from **Figure 2.1** that the lead atoms of plumbene monolayer are arranged in corrugated structure rather than flat structure of graphene. The cause of this corrugated structure is the hybridization of lead atoms between sp2 and sp3 [92]. δ is the vertical distance between atoms of the upper layer from that of the lower layer and d_1 is length of Pb−Pb bond. This type of corrugation virtually arranges the atoms into two layers in the thinner structure, so sometimes they are referred as bilayer of atoms instead of monolayer.

2.1.4 Methyl Decorated Plumbene Monolayer

After preparing the plumbene monolayer, next it is decorated with methyl (-CX_3, X = H, F, Cl) groups. The methyl groups can be easily obtained from organic alkane by chemical reaction [93]. Each lead atom of the monolayer is decorated with a single monovalent methyl group. The top and side views of the decorated structures have been shown in **Figure 2.2** (a) and (c).

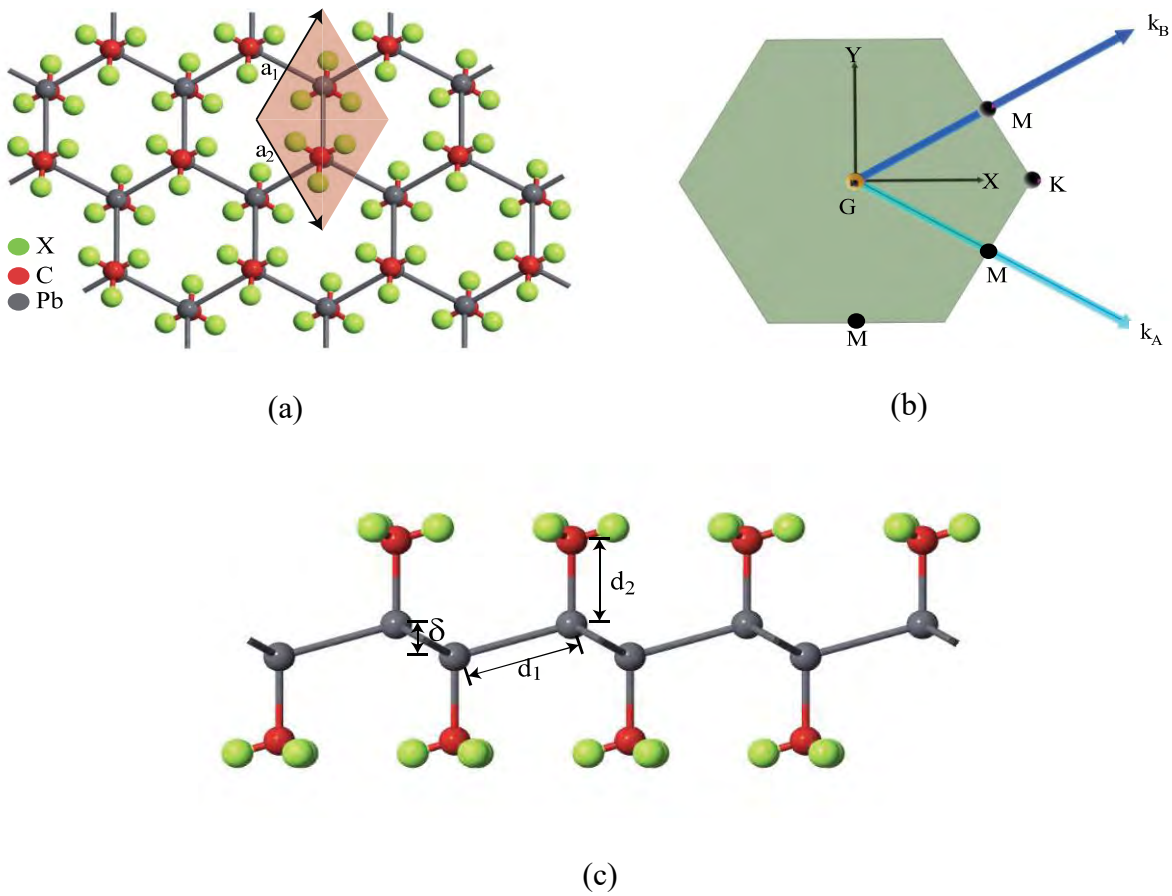

Figure 2.2 (a) Methyl decorated plumbene monolayer (top view) showing the unit cell with hexagonal crystal lattice, (b) Brillouin zone of the hexagonal crystal lattice with high symmetry points G, M, K, and (c) Side view of methyl decorated plumbene monolayer showing the Pb−Pb bond length (d_1), Pb−CX_3 bond length (d_2), buckling height (δ).

All the three groups used in decoration, methyl, trifluoromethyl and trichloromethyl are arranged in same pattern in the decorated plumbene monolayers with slight angle difference between the bonds. But in all the cases inversion symmetry is maintained in the single unit crystal cell of these materials.

The unit crystal cell has been marked by shadow. The Brillouin zone of the crystal unit cell is shown in **Figure 2.2** (b). From the Brillouin zone, we see a number of crystal symmetry points like G, M, K which keep a significant role in determining the topological invariant of quantum spin Hall insulator [94].

2.2 Determination of Electronic and Thermodynamic Stability

2.2.1 Calculation of Formation Energy

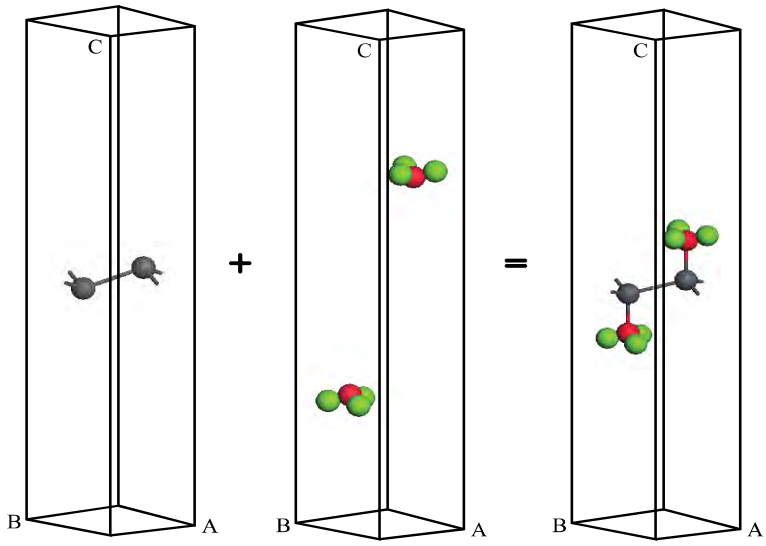

Figure 2.3 The methyl groups become attached to lead atoms of plumbene monolayer to form methyl decorated plumbene monolayer. The total energy of the methyl decorated plumbene monolayer should be less than the total energy of plumbene monolayer and isolated methyl groups to make the structure electronically stable.

In order to verify electronic stability of the decorated structures, the formation energy (ΔE) of each structure has been calculated from Equation (2.10).

$$\Delta E = E(PbCX_3) - E(Pb) - E(CX_3)\ , \qquad (2.10)$$

where $E(PbCX_3)$ and E(Pb) are the total energy of decorated and pristine plumbene nanosheet, respectively and $E(CX_3)$ is the chemical energy of methyl and trihalogenomethyl groups. The crystal cells for calculating the energies are shown in **Figure 2.3**.

2.2.2 Phonon Dispersion Curve

We have found the phonon dispersion curves of the crystal cells to determine the thermodynamic stability of each of the decorated monolayers. The phonon dispersion curves are obtained using CASTEP module in Materials Studio Software. The GGA-PBE functional is also used in this case and the pseudopotential used is OTFG ultrasoft. The frequency curve in phonon dispersion curve is found along every crystal momentum point. Analyzing phonon dispersion curve, it is possible to justify the material for its application at room temperature [95].

2.2.3 Molecular Dynamics Simulation

The molecular dynamics simulation has been done to show the method of chemical decoration in plumbene monolayer as well electronic and thermodynamic stabilities. This has been done in Quantumwise ATK using NPT Berendsen methodology. As there is no existing interaction potential for this novel system of materials, so we have performed the total quantum mechanical molecular dynamics simulation. The initial frame of the nanoribbon taken for molecular dynamic simulation is shown in **Figure 2.4**.

It is periodic along A direction of the lattice cell and the periodicity has been considered for computational efficiency. The time step between each frame of the molecular dynamic simulation

is 1femtosecond. The duration of molecular dynamics simulation is taken enough to observe the process of formation of bond and thermal vibration clearly.

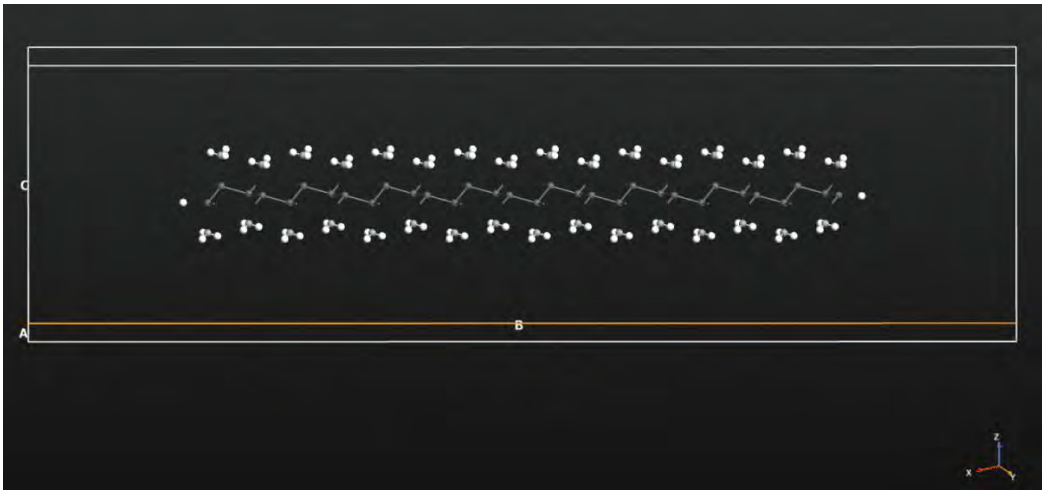

Figure 2.4 Initial frame for molecular dynamics simulation of $PbCH_3$ monolayer. The CH_3 groups are released to become attached to lead atom sites.

2.3 Quantum Spin Hall Insulators

2.3.1 Spin-Orbit Coupling and Bandgap Opening

Spin-orbit coupling is the interaction between magnetic field felt by an electron due to its orbital motion and magnetic moment due to its spin orientation [96]. An electron circles an atomic nucleus, as viewed from the frame of reference of the nucleus. From the electron's frame of reference, the nucleus is circling the electron as shown in **Figure 2.5 (a).** The circling nucleus produces a loop of current around the electron. The loop of the current produces a magnetic field whose magnitude and direction depends on the charge of nucleus and the direction of motion of electron. The magnetic field due to orbital motion interacts with magnetic moment due to spin of electron which gives rise to spin-orbit coupling.

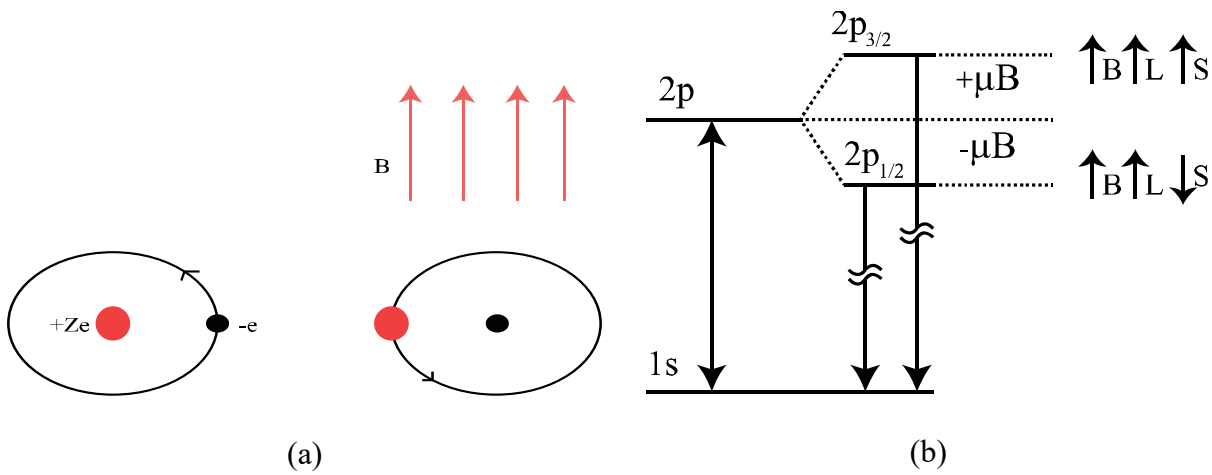

Figure 2.5 (a) An electron circles an atomic nucleus, as viewed from the frame of reference of the nucleus, from the electron's frame of reference, the nucleus is circling it. The magnetic field experienced by the electron as a result, is directed upward from the plane of the path of motion. The interaction between the electron's spin magnetic moment and this magnetic field leads to the phenomenon of spin-orbit coupling, (b) Energy level splitting of an orbital due to spin-orbit coupling.

Due to spin-orbit coupling the energy level is split between electrons with up and down spin by the amount of $2\mu B$ [97] shown in **Figure 2.5 (b)**, which is the cause of bandgap opening in group IV graphene analogue materials. Where, $\mu =$ the magnetic moment due to spin of electron and B = magnetic field felt by electron due to its orbital motion.

Thus, spin-orbit coupling increases in a group with the increase of atomic number Z, as the field B depends on the amount of charge in nucleus. So, in case of group IV graphene analogues, spin-orbit coupling increases as we go from top to bottom of the column. As a result, bandgap opening due to spin-orbit coupling increases as we move in that order.

2.3.2 Spin Hall Effect

Hall Effect is the phenomenon of building up of electrons on two sides of a material perpendicular to both the direction of the motion of charge and magnetic field, discovered by Edwin Hall in 1879 AD [98]. This happens due to magnetic force felt by charge which is given by Lorentz force, $F_m = q\bar{v} \times \bar{B}$. This occurs until the electric field force felt by an electron due to separation of charge is equal to the magnetic field force faced by it as shown in **Figure 2.6 (a)**.

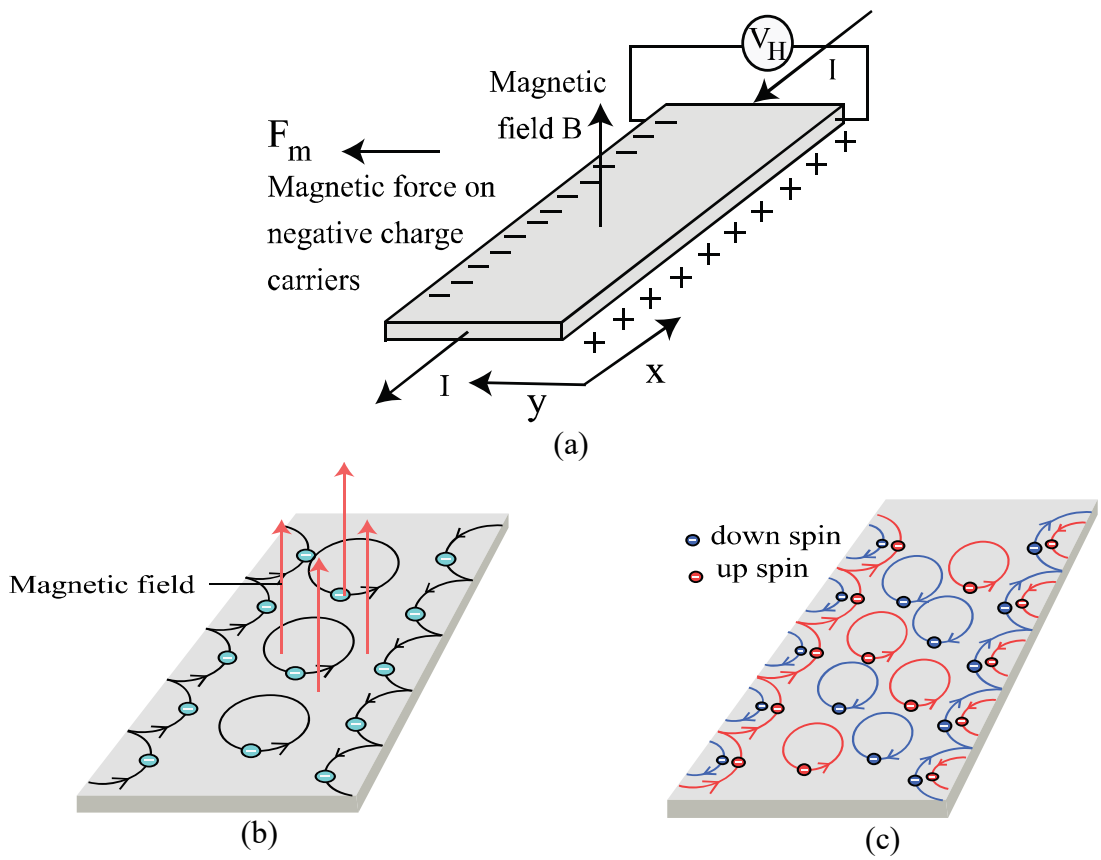

Figure 2.6 (a) The deposition of charges on two opposite sides perpendicular to both magnetic field and direction of motion of charge is due to Hall effect, (b) The increase of magnetic field leads to quantized conductance leading to quantum Hall effect, (c) The circling of electrons with up and down spins in two opposite directions leads to two edge states which is called quantum spin Hall effect.

Now, if the magnitude of magnetic field is very high, then electrons will not buildup at edges, rather they will move in small circles in the material, as magnetic field faced by electron is changing every moment due to change of its velocity. So, the electrons will become localized moving in small circles. But electrons at the edges will bounce through the edge and form dissipationless edge channels [**Figure 2.6** (b)] which is known as quantum Hall effect [9].

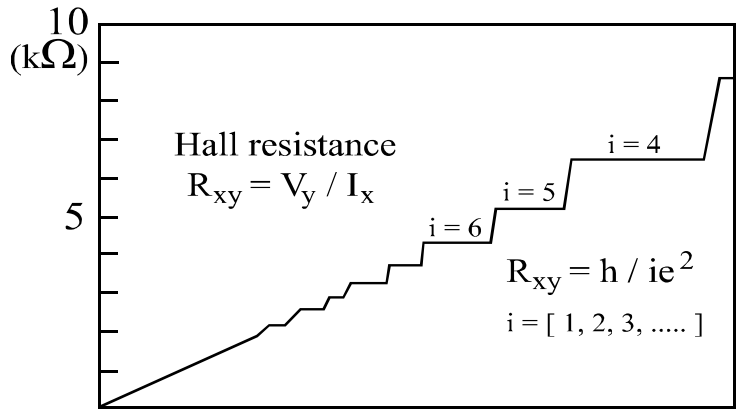

(a)

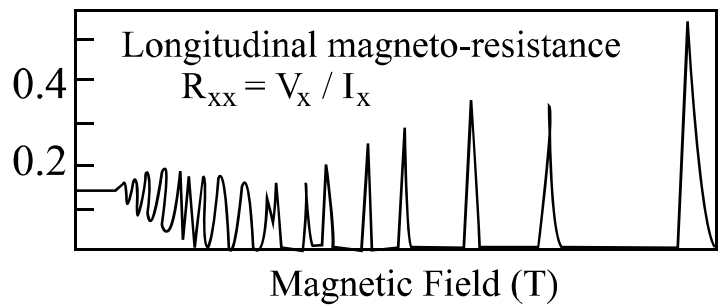

(b)

Figure 2.7 (a) The change of Hall resistance and Longitudinal magneto-resistance with change of magnetic field. The hall resistance increases linearly with magnetic field at first, but with increase of magnetic field it becomes quantized. (b) The longitudinal magneto-resistance remains constant irrespective of applied magnetic field at first, but at high magnetic field it becomes zero with some spikes at the time of transient.

The Hall resistance which is ratio of transverse voltage to longitudinal current is linear with applied magnetic field at low range but with the increase of magnetic field it is quantized as shown in **Figure 2.7** (a). The longitudinal magneto-resistance becomes zero with transient spikes at time of change of quantized levels [**Figure 2.7** (a)]. The problem in quantum Hall effect is that a large external magnetic field is required to build and maintain such dissipationless edge channels.

But, in materials with large spin-orbit coupling, the magnetic field faced by electrons due to orbital motion acts like this magnetic field, and electrons with up and down spin move in small circles in opposite directions as demonstrated in **Figure 2.6 (c)**. As a result, two dissipationless edge channels due to up and down spin electrons are formed at edges which move in opposite directions preserving time-reversal symmetry [99]. This is called quantum spin Hall effect, as spin of electrons is playing the major role in the formation of these type of edge states.

2.3.3 Time-Reversal Symmetry

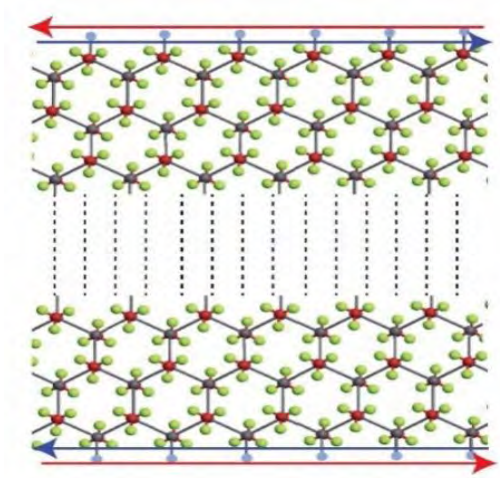

Figure 2.8 Topologically protected edge states due to time-reversal symmetry which determines the direction of motion of electron from its spin. If an electron wants to change its direction of motion, then it will have to change its spin, as spin uniquely determine the direction of motion.

Topological insulators have bulk bandgap like ordinary insulator and unique edge states protected by time-reversal symmetry [100]. Time-reversal symmetry allows the electrons with up and down spins to move in a particular direction along edges in quantum spin Hall insulators without scattering as shown in **Figure 2.8.** Due to time-reversal symmetry, an electron with up spin moving left-to-right, if faces any impurity, will not be able to move right-to-left, because if it wants to do so, then it will have to change its spin directly to down, which is not possible. So, electron along edge states of a quantum spin Hall insulators are protected against scattering from any non-magnetic impurity. This type of behavior prevents topological insulators from joule heating.

2.3.4 Z_2 Topological Invariant

A very important point about QSH phase is that, it is nontrivial. In that context, Kane and Mele further introduced a topological Z_2 invariant which characterizes a state as a trivial or nontrivial band insulator. Further studies of the robustness of the formed edge state proved both analytically and numerically that the nontrivial state is robust to both weak interactions and the extra spin-orbit coupling terms that mix spin-up and spin-down electrons.

Z_2 topological invariant in 2D materials differentiates between trivial insulator from quantum spin Hall insulator. There are two values of $Z_2 = 0$ or 1 for 2D topological insulators, which indicate trivial insulator or quantum spin Hall insulator respectively [94]. In 3D there are 4 values of Z_2 topological invariant, which differentiates between strong, weak topological insulator and trivial insulator [101]. In 2D materials, if edge states are protected by time-reversal symmetry that they are of Z_2 topological invariant 1. The electrons are not allowed to scatter back by impurity as the only scattering angle here is 180 degree **Figure 2.9** (a). So, there is no joule heating because of absence of scattering.

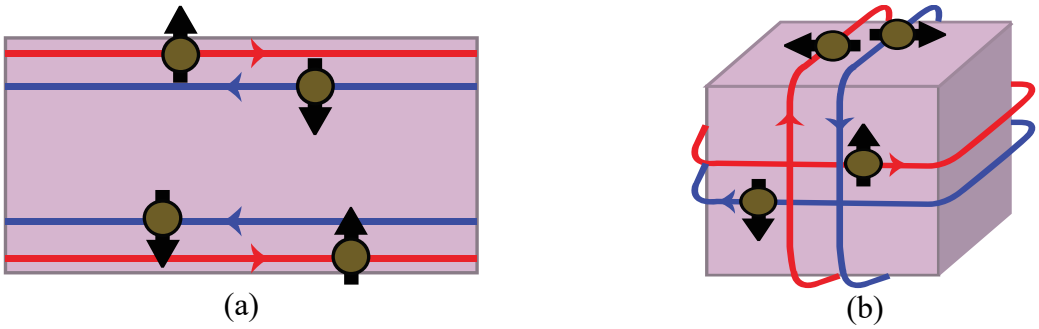

Figure 2.9 (a) Edge states in quantum spin Hall insulators showing the spin of electrons, (b) Surface states in 3D topological insulators with spin of electrons.

In 3D materials, it is possible to scatter at angles other than 180 degree [102] as electrons on the surface states have the opportunity to move any direction due to scattering as shown in **Figure 2.9** (b). So, there are 4 values of Z_2 topological invariant [94], differentiating between weak and strong topological insulators.

2.4 Determination of Topological Nontriviality

To find the topological nontriviality of the decorated structures, we have determined the $\mathbb{Z}_2$ topological invariant. The crystal cells of methyl decorated plumbene monolayers follow inversion symmetry. That means, the positions of all the atoms in the crystal cell are symmetric about the symmetry center [**Figure 2.10**].

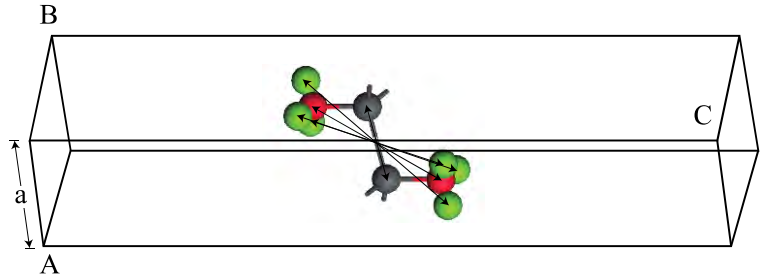

Figure 2.10 Crystal unit cell of methyl decorated plumbene monolayer ($PbCX_3$) showing inversion symmetry. Each atom has its image about the point of inversion symmetry.

For the crystal cell of a 2D topological insulator with inversion symmetry, topological invariants can be calculated from the symmetry of the Bloch function at four special Brillouin zone points given by Equation (2.11).

$$\Gamma_{i=(n_1,n_2)} = \frac{1}{2}(n_1 b_1 + n_2 b_2) \ , \tag{2.11}$$

where b_i are the reciprocal lattice vectors and $n_i = 0, 1$. For our case, the four special Brillouin zone points are G(0,0), M(0,0.5), M(0.5,0), M(0.5,0.5). These four points are time reversal invariant momentum (TRIM) points for 2D materials. The topological invariant can be calculated from the symmetry functions at the TRIM point, based on Kramer's theorem [103].

Now, assuming $\psi_{i,n}$ be the n-th occupied Bloch function at Γ_i point, the symmetry function can be calculated from the Equation (2.12), because of having inversion symmetry in the crystal structure of $PbCX_3$. $\langle\psi_{i,n}|\Theta|\psi_{i,n}\rangle$ represents the parity of n-th band at Γ_i TRIM point. Its value becomes −1 or +1 depending on whether the band is of odd or even parity. The number of Kramer's pair is indicated by this number.

$$\delta_i = \Pi_n \sqrt{\langle\psi_{i,n}|\Theta|\psi_{i,n}\rangle} \ , \tag{2.12}$$

Once symmetry functions at each Brillouin zone points are found, then topological invariant ν can be determined from Equation (2.13). The value of ν is 0 or 1, depending on the value of the product term.

$$(-1)^{\nu} = \Pi_{i=1}^{4} \delta_i \ . \tag{2.13}$$

If the value of ν is 0, then the material is topologically trivial insulator and if the value is 1, then the material is quantum spin Hall insulator.

2.5 Formation of Nanoribbon

To prove the existence of edge states and topological nontriviality, we have simulated nanoribbons (nanosheet with finite width) with zigzag edge pattern and obtained their bandstructures. The nanoribbon is periodic along x axis as shown in **Figure 2.11**. The edge dangling bonds are passivated by H atoms. The width of the nanoribbon along Y axis is 160 Å, which is sufficient to avoid the interaction between edge states.

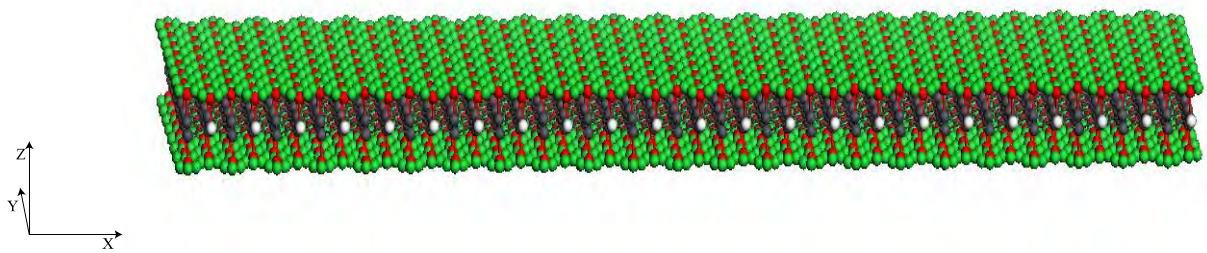

(a)

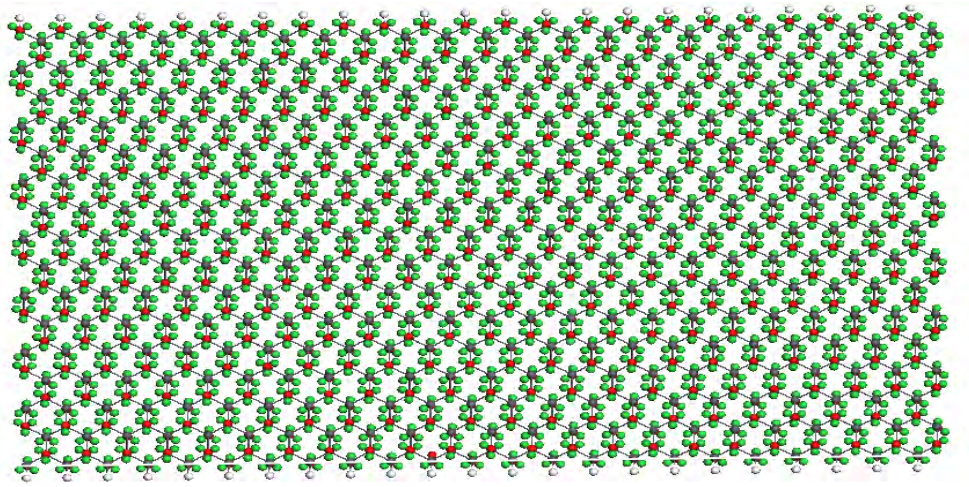

(b)

Figure 2.11 (a) $PbCH_3$ nanoribbon along zigzag direction. The dangling bond at the edge are passivated by hydrogen. (b) Top-view of the nanoribbon.

The Brillouin zone of the nanoribbon is sampled using 9×1×1 Gamma centered Monkhorst Package and the density mesh cutoff for the nanoribbon is set to 50 Hartree in this case. The nominal GGA-PBE functional is also used. The spin-orbit coupling effect is taken using the non-collinear spin-orbit coupling method. The structure for simulation is taken in such a way that only the minimum periodic part along x-direction is considered.

2.6 Application of Strain

In order to investigate the change of electronic properties with strain, we apply uniform biaxial strain to the crystal cell. Keeping the cell relaxed in C direction, the lattice parameter is reduced in A and B directions to apply compressive strain, and increased to apply tensile strain. This method of applying strain is generally used in studying the effect of strain on materials.

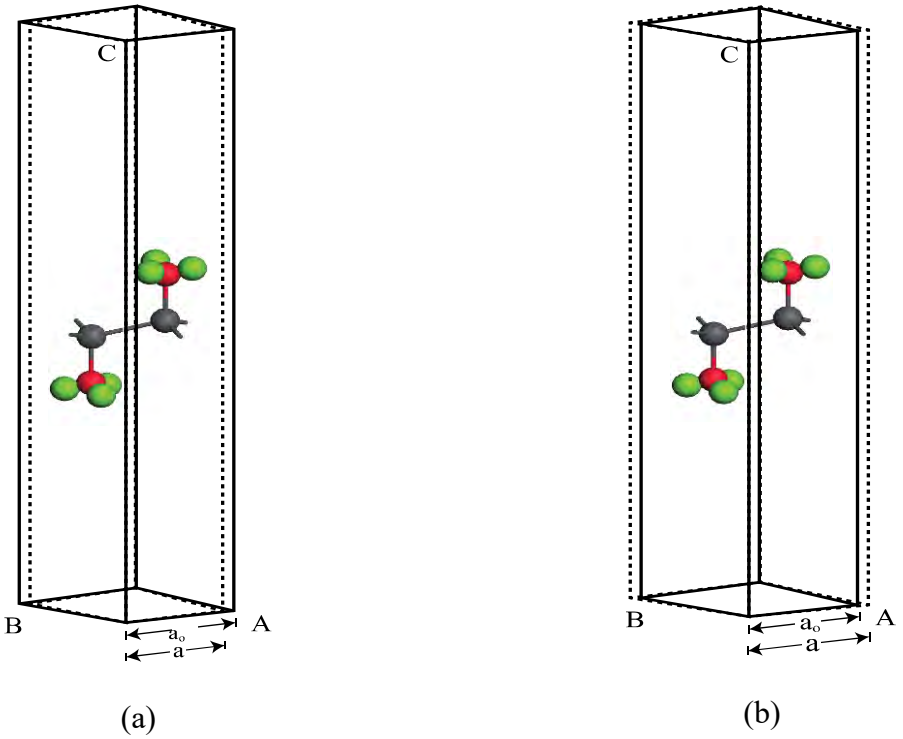

Figure 2.12 The method of applying strain to monolayer crystal cell. (a) Crystal cell after application of compressive strain, (b) Crystal cell after application of tensile strain.

Figure 2.12 shows the method of applying strain to the crystal cell. If the lattice parameter of the crystal cell without applying any strain is a_o and lattice parameter after applying strain is a then the amount of strain is $s = \frac{a-a_o}{a_o}$. Whether it is compressive or tensile strain depends on the sign of s. Then the atoms in the crystal cell is optimized after applying strain to have relaxed positions. After self-consistent simulation, the atoms take the relaxed positions.

The parameters used in geometry optimization and electronic properties calculation using strain are almost similar to that of the parameters used for normal optimization and electronic properties calculation.

Chapter 3

Chapter 3

Results and Topological Properties

3.1 Optimized Cells and Crystal Parameters

3.1.1 Optimized cells

The crystal cell of plumbene monolayer which is obtained by cleaving lead bulk structure, is decorated with methyl group after geometry optimization. **Figure 3.1** shows the geometry optimized crystal lattice cell of $PbCH_3$ monolayer.

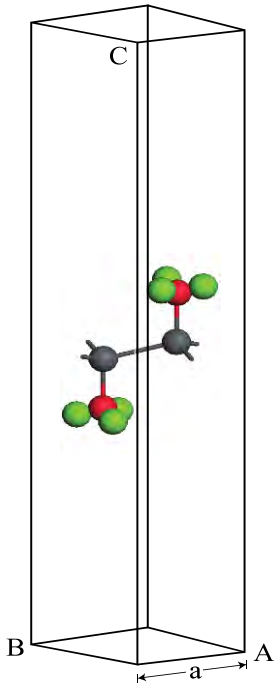

Figure 3.1 Crystal unit cell of methyl decorated plumbene monolayer ($PbCH_3$) after geometry optimization. The unit cell contains two lead atoms and two methyl groups.

The cell is periodic along A and B directions. A 30 Å vacuum distance is set along C direction so that adjacent monolayers do not interact with each other. The buckling height (δ) and Pb−CX_3

bond length (d_2) can be measured exactly from the relaxed coordinates of atoms in the crystal unit cell.

3.1.2 Crystal parameters

The results of geometry optimization and bandstructure calculation of methyl (CH_3) and trihalogenomethyl (CX_3) decorated plumbene nanosheets are summarized in **Table. 3-1**. It can be seen from the table, the buckling height (0.8863 Å) of the methyl (CH_3) substituted plumbene monolayer is higher compared to that of H-decorated monolayer (0.7781 Å) due to more dominant +I inductive effect of (CH_3) which assists in effective hybridization of π and σ orbitals. This also increases the mechanical stability of the methyl decorated plumbene monolayers.

Table. 3-1 Crystal lattice parameters (a) Pb−Pb bond length (d_1), Pb−CX_3 bond length (d_2), buckling height (δ_1), Energy bandgap with spin-orbit coupling (E_g), the formation energy (ΔE) and Z_2 topological invariant for different $PbCX_3$ monolayers.

Monolayer	a(Å)	d_1(Å)	d_2(Å)	δ_1(Å)	E_g (SOC)	ΔE(eV/atom)	$\mathbb{Z}_2$
Pb	4.92845	3.02	-	1.0071	0.3229	-	0
$PbCH_3$	5.07407	3.06	2.31	0.8863	0.9818	−1.3001	1
$PbCF_3$	5.12554	3.06	2.37	0.7904	0.9692	−2.42002	1
$PbCCl_3$	5.7454	3.34	2.40	0.406	0.841386	−1.70637	1

The buckling height suddenly decreases in case of –CCl_3 group due to more electronegativity of the group which attracts the π electrons towards it, and thus weakening the coupling between π and σ orbitals. The electronic stability of the structures is ensured from their formation energy ΔE using the Equation (2.10) in chapter 2, and the values obtained for $PbCH_3$, $PbCF_3$ and $PbCCl_3$ are

−1.3001eV/atom, −2.42002eV/atom and −1.70637 eV/atom respectively. The negative values of the formation energies indicate that there will be no phase separation between lead atoms (Pb) and methyl groups (CX_3) in $PbCX_3$.

3.2 Determination of Electronic and Thermodynamic Stability

3.2.1 Phonon Dispersion Curve

The thermodynamic stability is ensured from phonon dispersion curves of the decorated structures shown in **Figure 3.2**. The presence of no branch in the negative frequency region indicates that methyl, trifluoromethyl and trichloromethyl plumbene monolayer would be stable at room temperature.

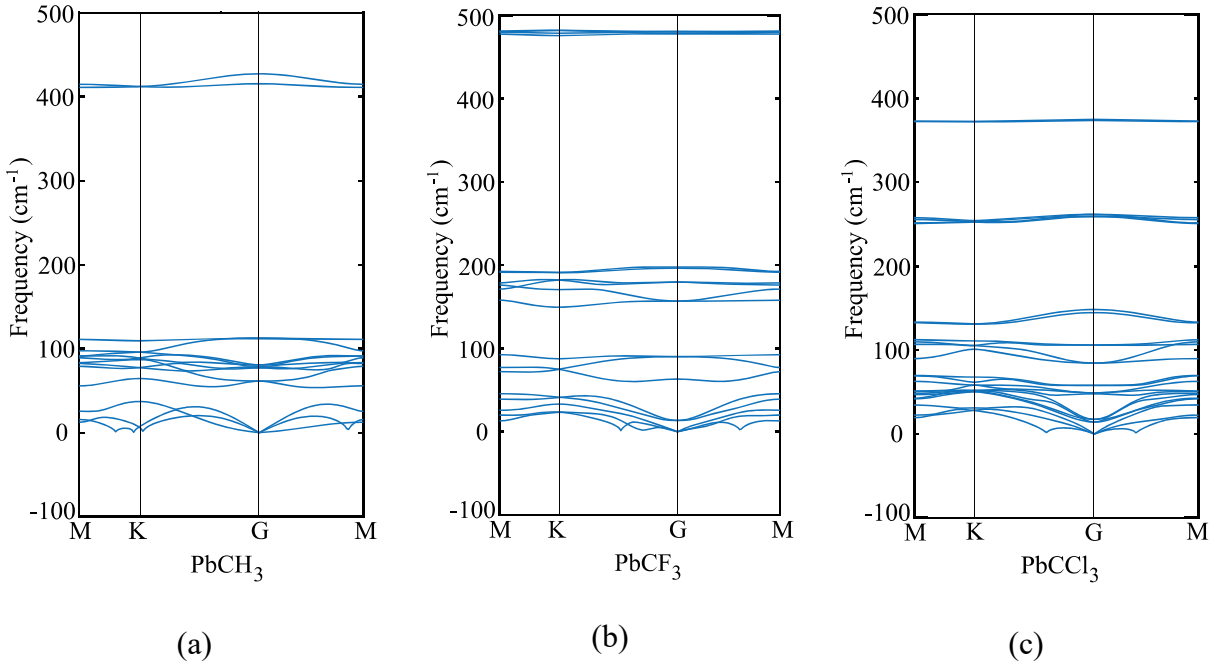

Figure 3.2 Phonon dispersion curves showing no branch in the negative frequency region and thermodynamic stability at room temperature. (a) $PbCH_3$ monolayer, (b) $PbCF_3$ monolayer and (c) $PbCCl_3$ monolayer.

3.2.2 Molecular Dynamics Simulation

The electronic and thermodynamic stability are also checked from molecular dynamics simulation [**Figure 3.3**]. **Figure 3.3** (a) and (c) show the initial and stable stages, respectively of molecular dynamics simulation for $PbCH_3$ nanoribbon. The nanoribbon is periodic in the direction perpendicular to the page. The CH_3 groups are placed at a distance of 3.53 Å from the plumbene nanoribbon at the initial step. **Figure 3.3** (b) shows the position of the atoms when the kinetic energy is maximum. From **Figure 3.3** (c), we observe that CH_3 groups nicely become attached with the lead atom sites and there is no broken bond at room temperature when stable structures are formed. **Figure 3.3** (d) shows the change of kinetic energy with respect to time for $PbCH_3$ materials.

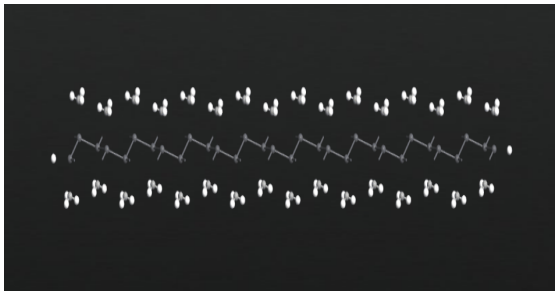

Time=0 ps

(a)

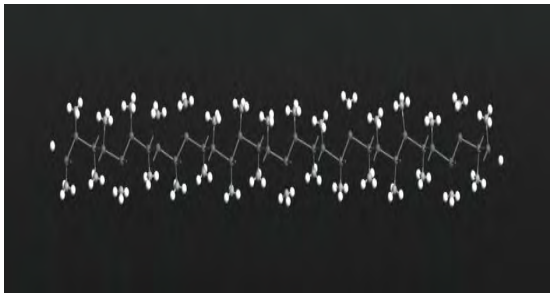

Time=0.054 ps

(b)

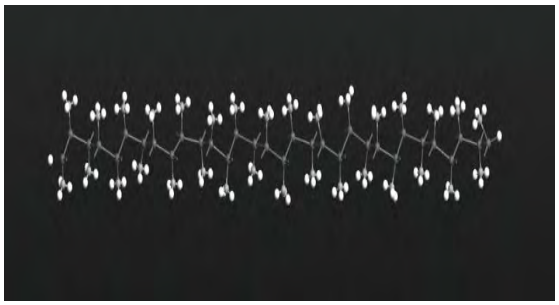

Time=0.454 ps

(c)

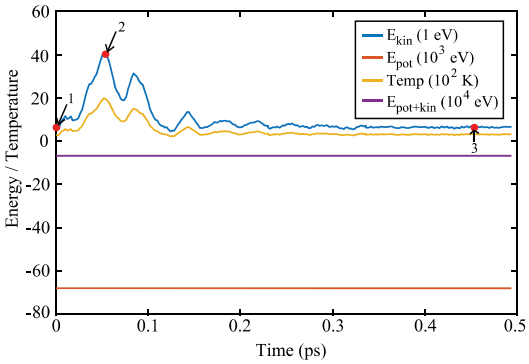

(d)

Figure 3.3 (a) The initial step (time = 0 ps) of molecular dynamics simulation of a $PbCH_3$ nanoribbon. It is periodic perpendicular to the page. (b) The stage of molecular simulation where CH_3 particles attain maximum kinetic energy (time = 0.054 ps), (c) The stable structure with no broken bond at room temperature (time=0.454 ps) and (d) Variation of system energy and temperature with respect to time. Red points, labelled as 1, 2 and 3, on the kinetic energy curve correspond to the position of the frames shown in (a), (b) and (c), respectively.

We see that the kinetic energy of the particles initially increases, and after forming the bonds, the system energy becomes stable where the atoms periodically oscillate without breaking any bond. Simulations are repeated for CF_3 and CCl_3 groups, and the corresponding energy curves and the final stable stages are shown in **Figure 3.4**. **Figure 3.4** (a) shows the energy curve for molecular dynamics simulation of $PbCF_3$ nanoribbon. From it we see that, the structure comes to a stable position at around 0.3 ps which is larger compared to that of $PbCH_3$ nanoribbon. The final relaxed structure with no breaking of bond has been shown in **Figure 3.4** (b). From energy curve of molecular dynamic simulation of $PbCCl_3$ nanoribbon in **Figure 3.4** (c), we see that the stable position is formed around 0.22 ps which is less than that of $PbCF_3$ nanoribbon but larger than that of $PbCH_3$ nanoribbon.

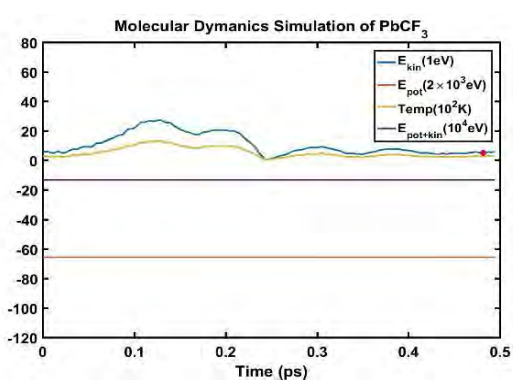

(a)

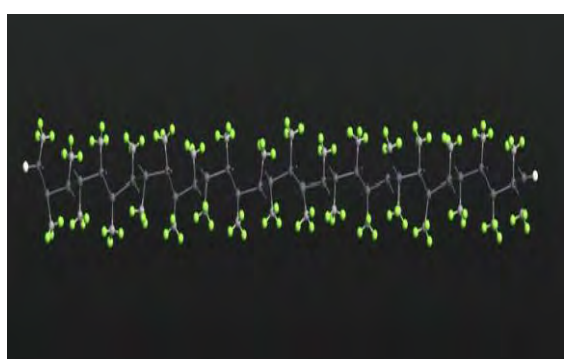

(b)

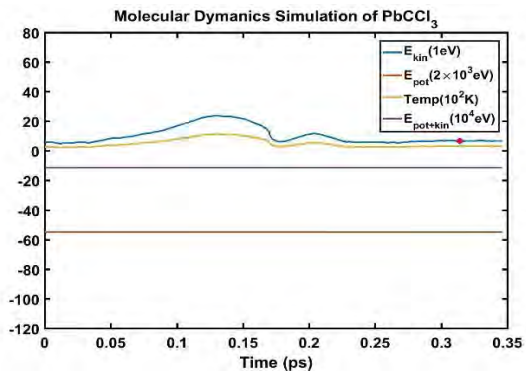

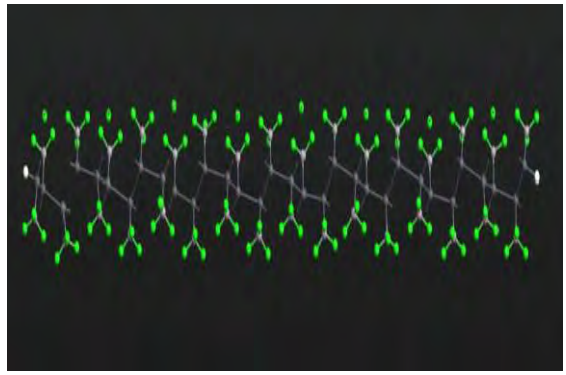

(c) (d)

Figure 3.4 (a) The energy curve for molecular dynamics simulation of $PbCF_3$ nanoribbon. The curve shows the gradual stable state of the nanoribbon, (b) The final stable nanoribbon showing no breaking of bond at room temperature, (c) the energy curve for MD simulation of $PbCCl_3$ nanoribbon, (d) The final stable nanoribbon of $PbCCl_3$ showing no breaking of bond at room temperature.

The final stable structure of $PbCCl_3$ nanoribbon without no breaking of bond has been shown in **Figure 3.4** (d).

We have also simulated the structural and electronic property of tribromomethyl plumbene ($PbCBr_3$) and triiodomethyl plumbene ($PbCI_3$) monolayers, but due to the lack of any definite stable geometric structure, and phase separation between plumbene and (CBr_3, CI_3), these materials have not been further considered for verification of topological properties.

3.3 Bandstructures and Partial density of states

3.3.1 Bandstructure

The bandstructure and partial density of states (PDOS) are calculated to observe the effect and origin of spin-orbit coupling. **Figure 3.5** (a) and (b) show the bandstructure of $PbCH_3$ monolayer crystal without and with spin-orbit coupling respectively.

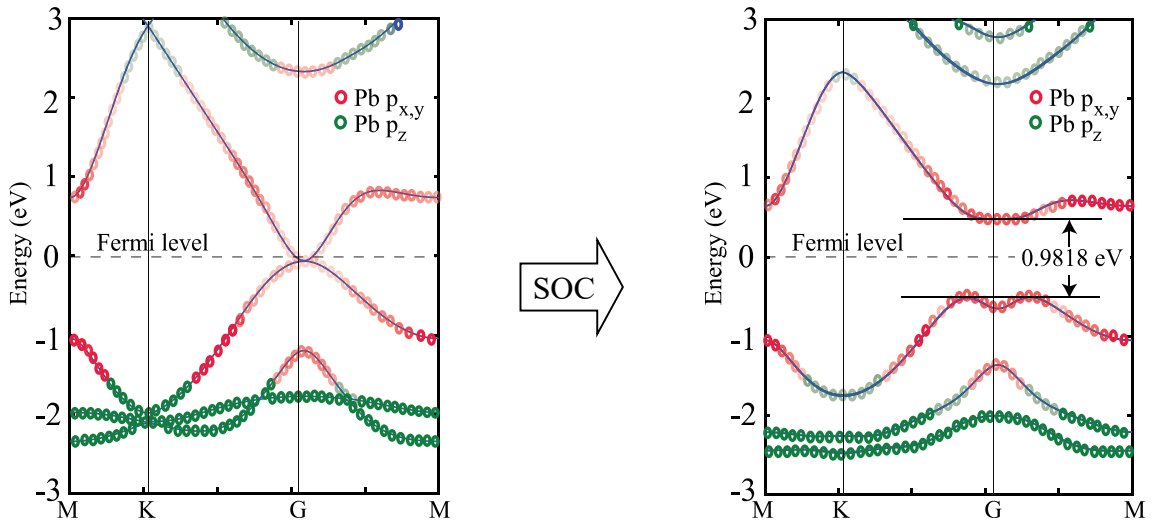

(a) (b)

Figure 3.5 (a) Bandstructure of the $PbCH_3$ monolayer showing the contribution of Pb $p_{x,y}$ and Pb p_z orbitals in forming the bands without spin-orbit coupling, (b) Bandstructure of the $PbCH_3$ monolayer with spin-orbit coupling.

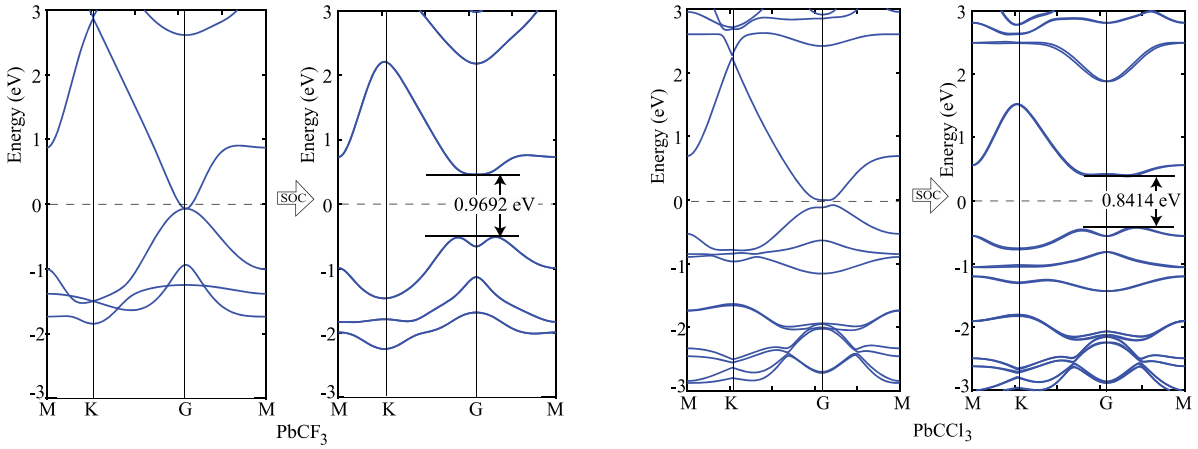

(a) (b)

Figure 3.6 (a) Bandstructure of $PbCF_3$ monolayer without and with spin-orbit coupling, (b) Bandstructure of $PbCCl_3$ monolayer without and with spin-orbit coupling.

The bandgap obtained for $PbCH_3$ taking the spin-orbit coupling into account is 0.9818 eV. The large bandgap for such a room temperature thermodynamic stable material is promising for quantum spin Hall insulator. The contribution of Pb $p_{x,y}$ and Pb p_z orbitals to each band of $PbCH_3$ are shown in colored red and green circles from which we see that the main contributions to valence and conduction bands near Fermi level are due to Pb $p_{x,y}$ orbitals.

Similar phenomena of the bandgap opening occurs for $PbCF_3$ and $PbCCl_3$ monolayer crystals, and the bandgaps obtained for $PbCF_3$ and $PbCCl_3$ with spin-orbit coupling are 0.9692eV and 0.8414eV respectively as shown in **Figure 3.6** (a) and (b). These range of bandgap are enough for room and high temperature application, as it is much higher than thermal energy of electron at room temperature (0.0259eV).

3.3.2 Verification of Bandgap with Hybrid Functional

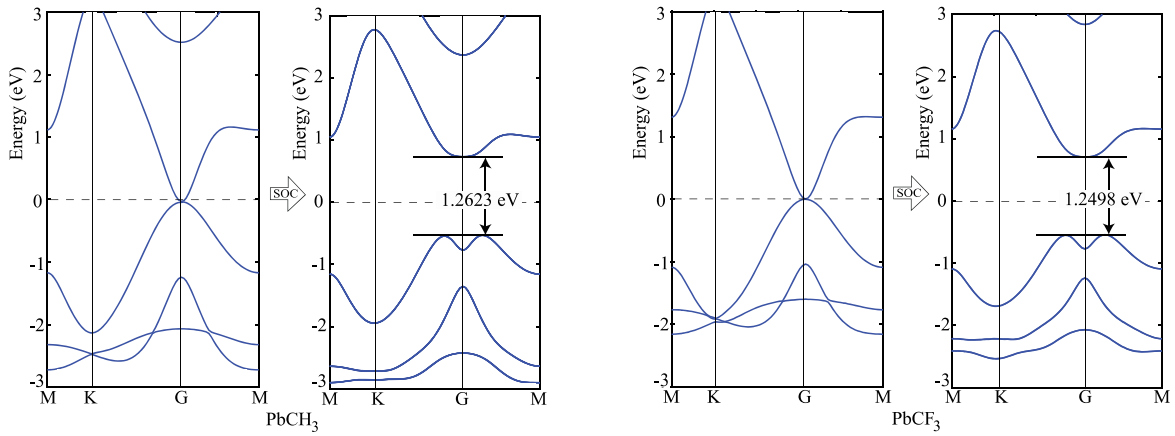

(a) (b)

Figure 3.7 Bandstructures without and with spin-orbit coupling employing HSE06 functional. (a) $PbCH_3$ monolayer (b) $PbCF_3$ monolayer.

To verify our simulation method, we have recalculated the electronic structures of $PbCH_3$ and $PbCF_3$ monolayers employing HSE06 functional. The bandstructures calculated for $PbCH_3$ and

$PbCF_3$ monolayers without and with spin-orbit coupling are shown in **Figure 3.7**. The bandgaps obtained for $PbCH_3$ and $PbCF_3$ monolayers using this method are found to be 1.2623eV and 1.2498eV respectively. As GGA-PBE is known to underestimate the bandgaps, the bandstructures obtained from HSE06 functional are consistent with those obtained from GGA-PBE.

3.3.3 Partial Density of States

The partial density of states shows the contribution of atomic orbitals to the bandgap. Observing the contribution of orbitals from partial density of states in **Figure 3.8** (a) and (b), we see that when spin-orbit coupling is introduced, the degeneracy of Pb $p_{x,y}$ orbitals causes the bandgap opening near Fermi level. The lower bands are due to the contribution from Pb p_z orbital. The partial density of states in $PbCF_3$ monolayer without and with spin-orbit coupling are shown in **Figure 3.8** (c) and (d) respectively.

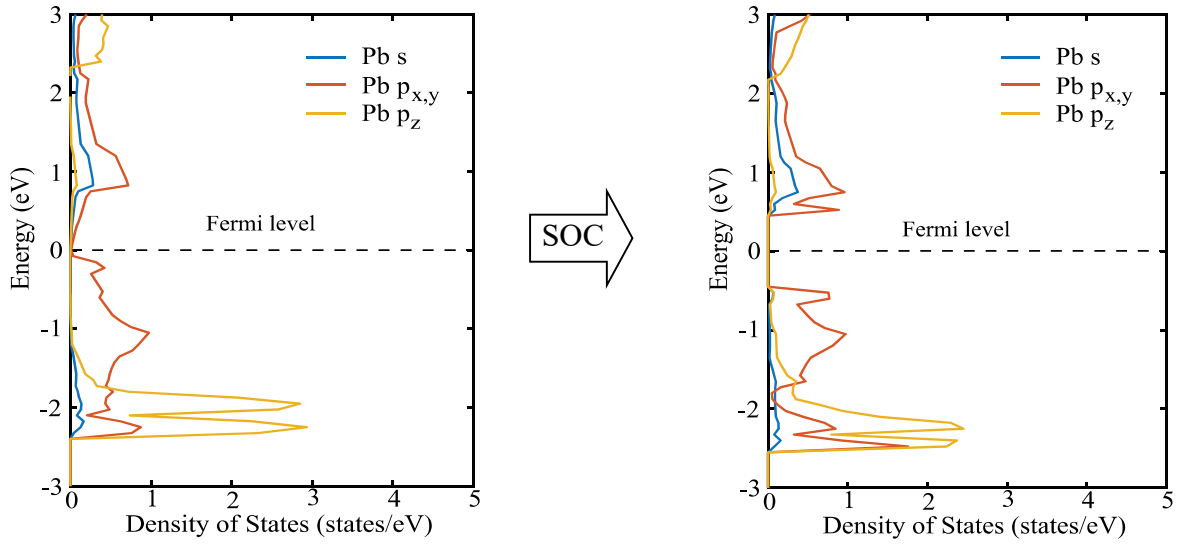

(a) (b)

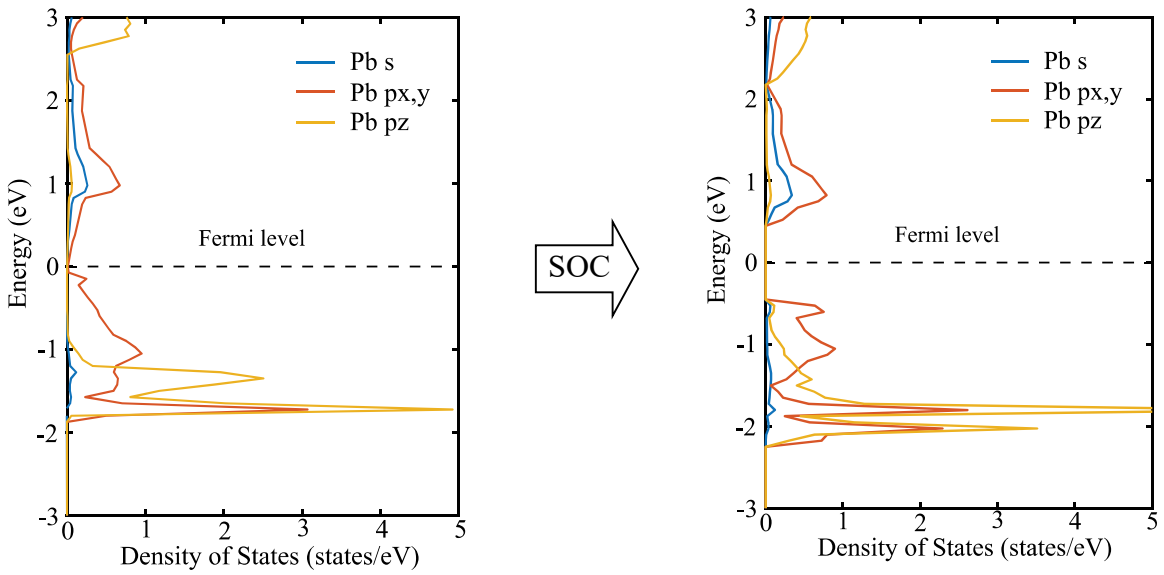

(c) (d)

Figure 3.8 (a) Partial density of states showing the contributions of Pb s, Pb $p_{x,y}$ and Pb p_z orbitals without spin-orbit coupling in $PbCH_3$ (b) Partial density of states with spin-orbit coupling. From the figures, it is seen that the major contribution to the bands near to Fermi level is due to Pb $p_{x,y}$ orbitals. (c) Partial density of states without spin-orbit coupling in $PbCF_3$, (d) Partial density of states with spin-orbit coupling in $PbCF_3$.

3.4 Topological Invariant and Orbital Analysis

3.4.1 Topological Invariant

The effect of spin-orbit coupling leads to the formation of edge states and these edge states will have to be topologically protected against backscattering. The robustness of these edge states against backscattering is determined from topologically invariant property. Thus, to find the robustness of the edge states, we have calculated the topological $\mathbb{Z}_2$ invariant of the each monolayer. For example, if we consider $PbCH_3$ monolayer, there are 4 valence electrons in the outer shell of Pb, C and 1 valence electron in hydrogen. Hence, the total number of valence

electrons in each crystal lattice shell is 2 × (4 + 4 + 3 × 1) = 22. By calculating the $\langle \psi_{i,n} | \Theta | \psi_{i,n} \rangle$ at the 2mth occupied band, we have found the symmetry function δ_i at each symmetry points G(0,0), M(0,0.5), M(0.5,0) and M(0.5,0.5). As values of $\langle \psi_{i,n} | \Theta | \psi_{i,n} \rangle$ at the 2m−1th and 2mth bands are same due to spin degeneracy, the product of $\sqrt{\langle \psi_{i,n} | \Theta | \psi_{i,n} \rangle}$ at the 2m−1th and 2mth bands $\left(\prod_{2m-1}^{2m} \sqrt{\langle \psi_{i,n} | \Theta | \psi_{i,n} \rangle} \right)$ is essentially the same as the value of $\langle \psi_{i,n} | \Theta | \psi_{i,n} \rangle$ at the 2mth band. Then, the topological invariant is calculated using equation (4), as shown in **Table. 3-2** and the $\mathbb{Z}_2$ topological invariant with ν = 1 indicates the topological nontriviality.

Table. 3-2 Parities of 11 occupied spin-degenerated bands and symmetry functions at each symmetry points. The even and odd parities are represented by + and − signs.

Γ_i	$\langle \psi_{i,n} \mid \Theta \mid \psi_{i,n} \rangle$ **of 2mth occupied band**	δ_i
(0,0)	− − + + − + − + − + −	+
(0.5,0)	+ − + − + − + − + − +	−
(0,0.5)	+ − + − + − + − + − +	−
(0.5,0.5)	+ − + − + − + − − + +	−
$PbCH_3$	$\mathbb{Z}_2$ topological invariant	ν = 1

3.4.2 Orbital Analysis

To get a clear understanding of the origin of bandgap and topological nontriviality, we have presented the methodical band evolution at G point for $PbCH_3$ in **Figure 3.9**. Analyzing the bandstructure and partial density of states in **Figure 3.5** and **Figure 3.8**, we have done an orbital analysis to investigate the origin of topological characteristics. From partial density of states

(PDOS) of $PbCH_3$ in **Figure 3.8**, we see that the Pb s and Pb $p_{x,y}$ orbitals dominate the valence and conduction bands near the Fermi level. When chemical bonding is formed between Pb−Pb atoms, then effect of crystal field splitting creates bonding states and anti-bonding states for the s and $p_{x,y}$ orbitals, which we have denoted with $|s\pm\rangle$ and $|p_{x,y},\pm\rangle$, where + and − represent the parities of the corresponding state respectively. As displayed in **Figure 3.9**, the bands near the Fermi level are due to $|p_{x,y},\pm\rangle$ in absence of spin-orbit coupling (SOC). When the spin-orbit coupling is included in the calculation, the degeneracy of the level splits into $|p_{x,y},\pm 3/2\rangle$ states with a total angular momentum j=3/2 and $|p_{x,y},\pm 1/2\rangle$ with a total angular momentum j = 1/2, creating an energy gap at the G point. Similar analysis can be done and same conclusion can be drawn for $PbCCl_3$ and $PbCF_3$.

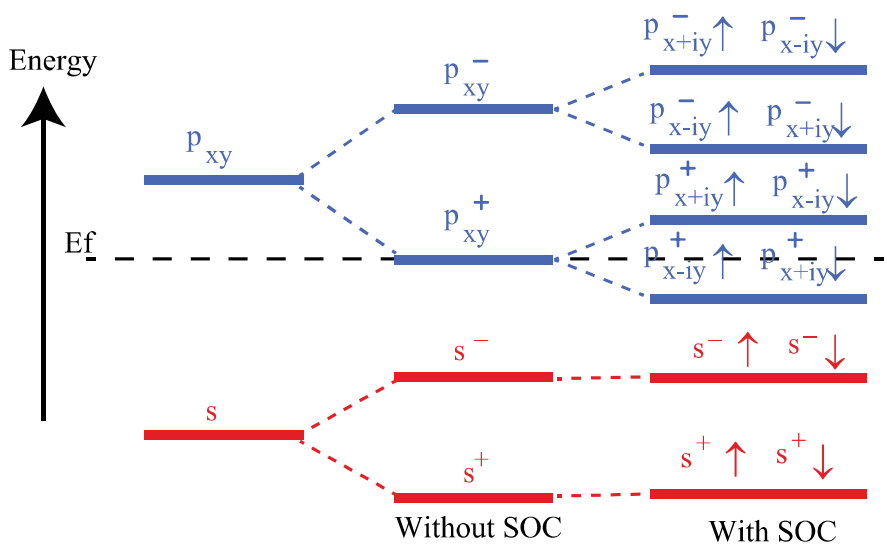

Figure 3.9 The orbital analysis of $PbCH_3$ at G(0,0) point, which shows that contribution of s and $p_{x,y}$ atomic orbitals to bands near Fermi level. The bandstructure formation is mainly due to crystal field splitting and spin-orbit coupling.

3.5 Analysis of Nanoribbon

The presence of edge states and topological invariant can be clearly observed if we construct a semi-infinite $PbCH_3$ sheet and investigate its bandstructure. We simulate the semi-infinite nanoribbons of each materials as shown in **Figure 3.10** (a). The nanoribbon has edges in the zigzag direction and the dangling bonds at the edges are passivated by hydrogen atoms. **Figure 3.10** (b) shows the corresponding bandstructure of $PbCH_3$ nanoribbon. Here, there are two symmetry points Z and X in the Brillouin zone of the nanoribbon due to its periodicity along A direction. We see from the bandstructure that the nanoribbon is insulating in the bulk except there is a pair of edge states along the edges which is observed by the presence of certain bands in the bandgap region. The contribution of spins to the edge states at bandgap region can be obtained from Kramer's theorem which states that every time reversal invariant momentum (TRIM) is doubly degenerate.

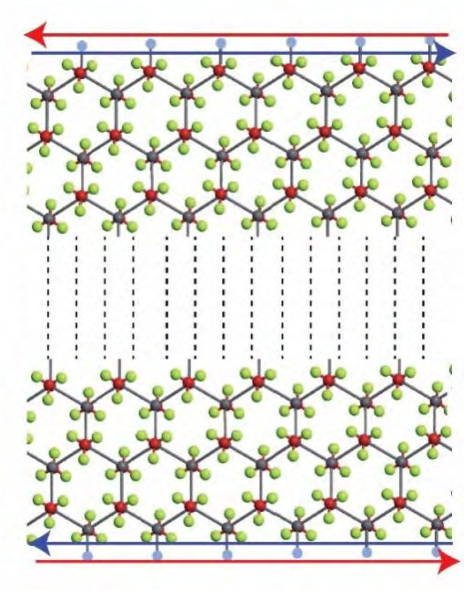

(a)

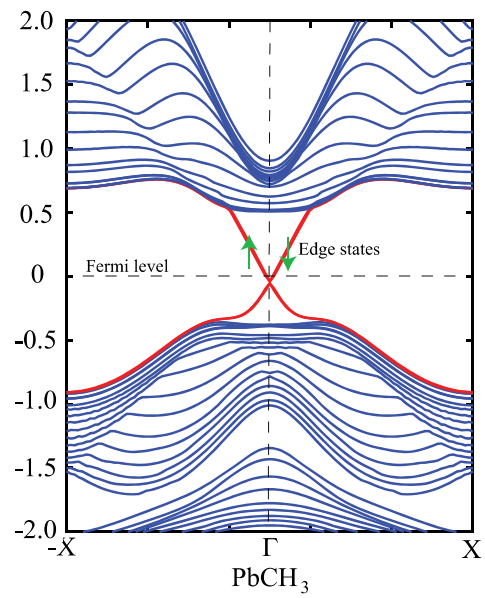

(b)

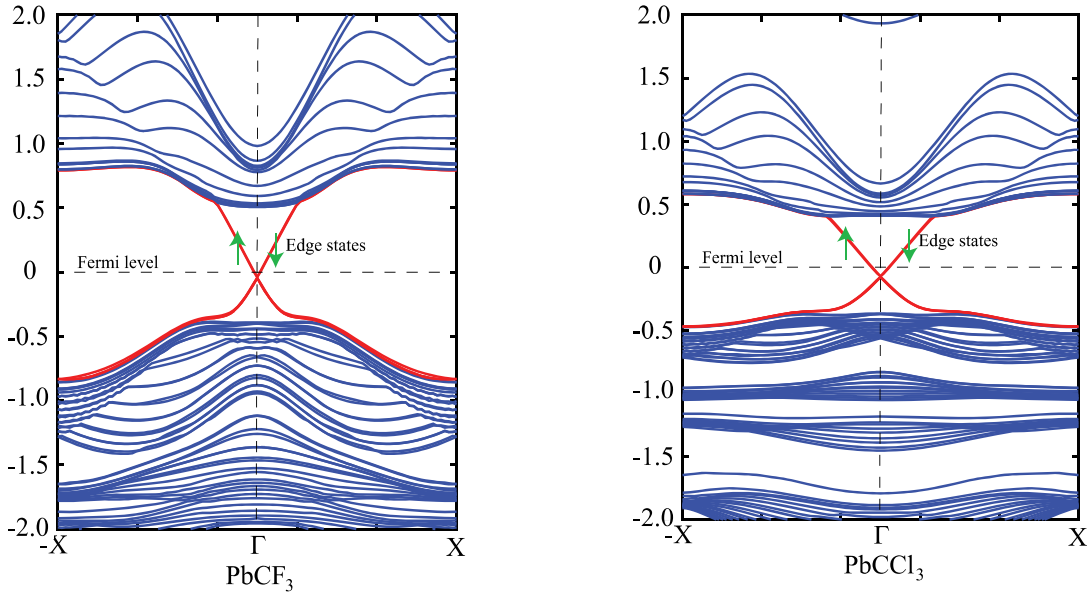

(c) (d)

Figure 3.10 (a) $PbCH_3$ nanoribbon along zigzag direction. The dangling bonds at the edges are passivated by hydrogen. The blue and red colors arrows represent the edge states due to up and down spin respectively. (b) Bandstructure of zigzag $PbCH_3$ nanoribbon showing odd number of band passing through Fermi level which proves the Z_2 topological invariant of 1. The red color band corresponds to the bands due to edge states. (c) Bandstructure of zigzag $PbCF_3$ nanoribbon. (d) Bandstructure of zigzag $PbCCl_3$ nanoribbon.

3.5.1 Determination of Topological Invariant

The Topological invariant of the edge states can be calculated from the number of bands that are crossing Fermi level from Γ to X point. From **Figure 3.10** (b), (c) and (d), we see that the number of bands crossing Fermi level from Γ to X point is 1 which is an odd integer. So, it can be told that the edge states are protected by time-reversal symmetry.

3.5.2 Determination of Fermi velocity

The Fermi velocity obtained for electrons in $PbCH_3$ nanoribbon is 7.38×10^5 ms^{-1} as calculated from **Figure 3.10** (b) using the formula $E = \hbar v_f k$, suggests its possible application in high speed electronics. Same phenomena were observed in the bandstructures of $PbCF_3$ and $PbCCl_3$ nanoribbons in **Figure 3.10** (c) and **Figure 3.10** (d).

3.6 Change of Properties with Strain

3.6.1 Stability and Change of Bandgap

In order to investigate the stability of the materials and change of properties with the change of strain (±4%), we have shown the variation of bandgap and formation energy versus strain. From **Figure 3.11** (a), we see that the bandgap of $PbCH_3$ decreases gradually with the increase of strain and increases upto compressive strain of 4%. The formation energies in the negative region, shown by **Figure 3.11** (b), ensures the electronic stability of the materials under strain. The bandgap vs strain curve of $PbCF_3$ is almost linear in the total range of strain. It has been previously discussed that bandgap opens mainly due to p-p orbital splitting with spin-orbit coupling. Thus, the reason behind the strain-dependent variation of bandgaps can be found from orbital analysis. **Figure 3.11** (c) shows that the p-p orbital splitting decreases with compressive strain and increases with the increase of tensile strain, and the bandgaps follow the trend accordingly. We have not applied strain more than 4% because beyond that it leads to structural deformation. Thus, changing the strain in methyl and trihalogenomethyl decorated plumbene monolayer, topological insulators with much higher bandgap may be obtained.

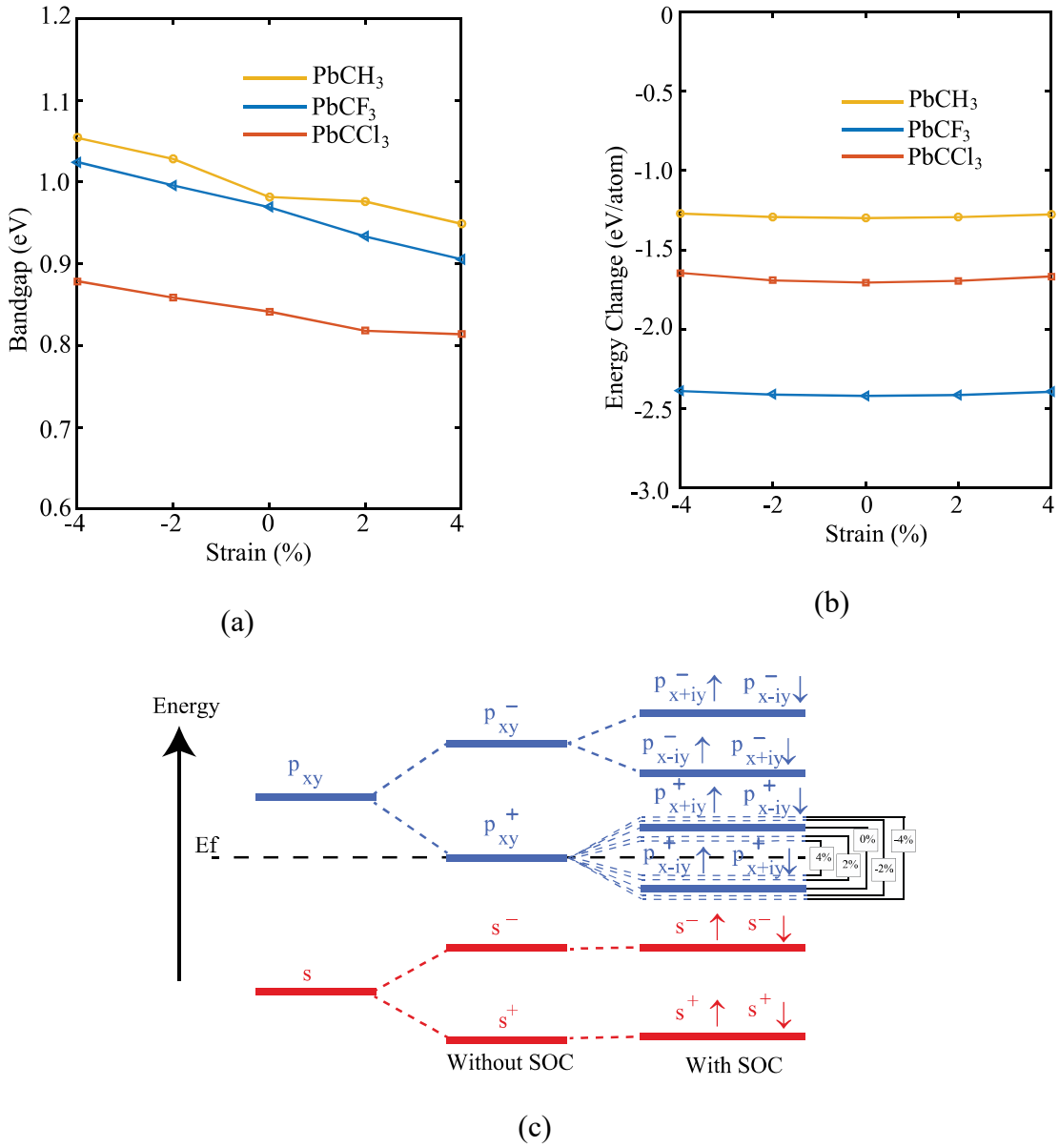

Figure 3.11 (a) The change of bandgap (E_g) taking the effect of spin-orbit coupling (SOC) with change of strain, (b) the change of formation energy ΔE with strain. The negative values of formation energies ensure electronic stability. (c) The orbital analysis of $PbCH_3$ at G(0,0) point for different percentages of strain, which shows that contribution of s and $p_{x,y}$ atomic orbitals to bands near Fermi level. The amount of splitting in p-p orbitals is changed as shown by the dotted lines.

3.6.2 Change of Bond Length

The buckling height increases with increase of application of compressive strain. The change of buckling height and Pb-Pb bond distance with change of strain is shown in **Figure 3.12**.

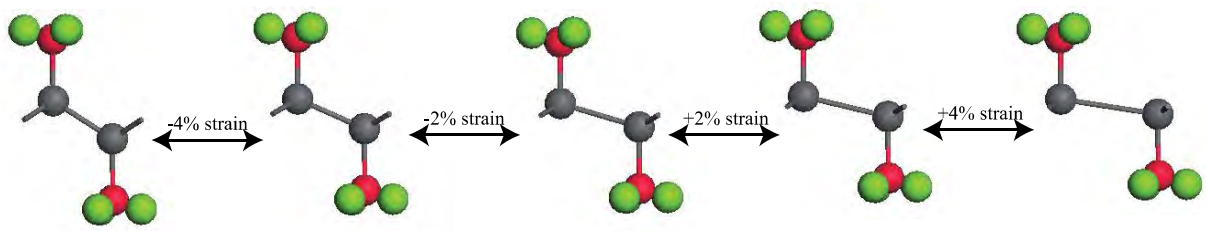

Figure 3.12 Change of buckling height (δ) and Pb−Pb (d_1) bond distance in $PbCH_3$ crystal cell with application of tensile and compressive strain. There is almost no change shown in the Pb−CH_3 atoms.

Table. 3-3 shows the change of different types of bond length with change of strain. We see that buckling height (δ_1) increases in case of all the monolayer crystal cells with application of compressive strain and it decreases with application of tensile strain. The Pb−Pb bond length (d_1) decreases with application of compressive strain and increases with tensile strain. The Pb−CX_3 bond length remains almost unchanged with application of strain. Beyond +4% strain, the distance between lead atoms becomes too large to form covalent bond. So, strain beyond +4% causes deformation of the crystal cell. Below −4% strain, the atoms are closed enough to interact with each other to distort the electronic properties. If compressive strain is too much, then interaction of atoms sometimes causes the self-consistent simulation to be failed.

Table. 3-3 Change of different types of bond lengths with the change of strain

Amount of Strain	Buckling Height δ_1(Å)			Pb−Pb Bond Length d_1(Å)			Pb−CX_3 Bond Length d_2(Å)		
Materials	$PbCH_3$	$PbCF_3$	$PbCCl_3$	$PbCH_3$	$PbCF_3$	$PbCCl_3$	$PbCH_3$	$PbCF_3$	$PbCCl_3$
-4%	0.9816	0.9136	0.7028	2.99	2.98	3.23	2.32	2.38	2.42
-2%	0.9293	0.8412	0.5481	3.04	3.02	3.28	2.31	2.38	2.41
0%	0.8863	0.7904	0.406	3.06	3.06	3.34	2.31	2.37	2.40
2%	0.6258	0.6312	0.2812	3.10	3.11	3.39	2.30	2.36	2.40
4%	0.4125	0.4261	0.1647	3.14	3.17	3.45	2.30	2.35	2.39

Chapter 4 Conclusion and Future Works

Chapter 4

Conclusion and Future Works

4.1 Conclusion

We have predicted a new family of methyl and trihalogenomethyl decorated plumbene monolayers, as large bandgap quantum spin Hall insulators, showing excellent topological property at room temperature. The electronic and thermodynamic stabilities of these materials have been checked from phonon dispersion curve and molecular dynamics simulation, making its place for room temperature application. Orbital analysis shows that the bandgap opening is mainly due to p−p band splitting caused by spin-orbit coupling. The $\mathbb{Z}_2$ topological invariant confirms the robustness of edge states against backscattering that is protected by time-reversal symmetry. The presence of bands in the bandgap region of the bandstructure obtained by simulating nanoribbons, further confirms the presence of edge states and its topological nontriviality. We have also seen its structural stability against externally applied strain, which enhances the possibility of obtaining topological insulators with higher bandgaps using strain. These findings demonstrate that the methyl and trihalogenomethyl decorated Pb films may be good QSH platforms for the design of topological electronic devices, spintronics and dissipationless electronic transport.

4.2 Future Works

We have proved methyl and trihalogenomethyl decorated plumbene monolayers as quantum spin Hall insulators. We think, there is still some scope of novel research on these type of materials system.

1. To investigate whether methyl decorated plumbene monolayers can be used as channel materials in transistor. Though in quantum spin Hall insulators, there is vanishing charge-conductance but it can be avoided if the time-reversal symmetry is broken using magnetic impurity leading to quantum anomalous Hall effect. These materials can be used as channel materials due to their high electron mobility.

2. To evaluate the performance of methyl decorated plumbene monolayers in generating spin current and applying spin-orbit torque. As magnetic circuit offers low-power electronic devices, so these materials can be used to generate large spin current. These materials can also be used to change magnetization of a materials, as these can apply a high spin-orbit torque.

3. To find out the layer-dependent properties and performance of these materials against defects and impurities. Edge states of quantum spin Hall insulators are protected by time-reversal symmetry. Also there is difficulty in growing monolayer materials, so the performance of these materials with change of layer can be investigated.

4. The methodology used here can be projected to find 3D topological insulators. 3D topological insulators are particularly fascinating due to high spin-orbit torque.

References

[1] Hasan, M.Z. and C.L. Kane, "Colloquium: Topological Insulators," *Reviews of Modern Physics*, vol. 82, no. 4, p. 3045, 2010.

[2] Cava, R.J., et al., "Crystal Structure and Chemistry of Topological Insulators," *Journal of Materials Chemistry C*, vol. 1, no. 19, pp. 3176-3189, 2013.

[3] Kane, C.L. and E.J. Mele, "Z2 topological Order and the Quantum Spin Hall Effect," *Physical Review Letters*, vol. 95, no. 14, p. 146802, 2005.

[4] Zhao, H., et al., "Prediction of Tunable Quantum Spin Hall Effect in Methyl-Functionalized Tin Film," *Journal of Materials Chemistry C*, vol. 5, no. 10, pp. 2656-2661, 2017.

[5] Klitzing, K. V., Dorda, G., and Pepper, M., “New method for high-accuracy determination of the fine-structure constant based on quantized Hall resistance”, *Physical Review Letters*, vol. 45, no. 6, pp. 494-497, 1980.

[6] Kane, C.L. and E.J. Mele, "Quantum Spin Hall Effect in Graphene," *Physical Review Letters*, vol. 95, no. 22, p. 226801, 2005.

[7] Novoselov, K.S., Geim, A.K., Morozov, S.V., Jiang, D., Zhang, Y., Dubonos, S.V., Grigorieva, I.V., and Firsov, A.A., "Electric field effect in atomically thin carbon films," *Science*, vol. 306, no. 5696, pp. 666-669, 2004.

[8] Geim, A.K., and Novoselov, K.S., “The Rise of Graphene”, *Nature Materials*, vol. **6**, no. 3, pp. 183-191, 2007.

[9] Haldane, F.D.M., "Model for a Quantum Hall Effect without Landau Levels: Condensed-Matter Realization of the "Parity Anomaly*",*" *Physical Review Letters*, vol. 61, no. 18, pp. 2015-1-2015-4, 1988.

[10] König, M., et al., "Quantum Spin Hall Insulator State in HgTe Quantum Wells," *Science*, vol. 318, no. 5851, pp. 766-770, 2017.

[11] Knez, I., R.-R. Du, and G. Sullivan, "Evidence For Helical Edge Modes in Inverted InAs/GaSb Quantum Wells," *Physical Review Letters*, vol. 107, no. 13, p. 136603, 2011.

[12] König, M., Wiedmann, S., Brüne, C.,Roth, A., Buhmann, H., Molenkamp, L.W., Qi, X.L., and Zhang, S.C., "Quantum Spin Hall Insulator State in HgTe Quantum Wells," *Science*, vol. 318, no. 5851, pp. 766-770, 2007.

[13] Qian, X., Liu, J., Fu, L. and Li, J., "Quantum Spin Hall Effect and Topological Field Effect Transistor in Two-Dimensional Transition Metal Dichalcogenides," *Science*, vol. 346, pp.1344-1347, 2014.

[14] Zhou, L., Kou, L., Sun, Y., Felser, C., Hu, F., Shan, G., Smith, S.C., Yan, B. and Frauenheim, T., "New Family of Quantum Spin Hall Insulators in Two-Dimensional Transition-Metal Halide with Large Nontrivial Bandgaps," *Nano Letters*, vol. 15, no. 12, pp. 7867-7872, 2015.

[15] Liu, P.F., Zhou, L., Frauenheim, T. and Wu, L.M., "New Quantum Spin Hall Insulator in Two-Dimensional MoS_2 with Periodically Distributed Pores," *Nanoscale*, vol. 8, no. 9, pp. 4915-4921, 2016.

[16] Zheng, F., Cai, C., Ge, S., Zhang, X., Liu, X., Lu, H., Zhang, Y., Qiu, J., Taniguchi, T., Watanabe, K. and Jia, S., "On the Quantum Spin Hall Gap of Monolayer 1T′-WTe_2," *Advanced Materials*, vol. 28, no. 24, pp. 4845-4851, 2016.

[17] Lüpke, F., Waters, D., Sergio, C., Widom, M., Mandrus, D.G., Yan, J., Feenstra, R.M. and Hunt, B.M., "Proximity-Induced Superconducting Gap in the Quantum Spin Hall Edge State of Monolayer WTe_2," *Nature Physics*, vol. 16, no. 5, pp. 526-530, 2020.

[18] Chen, P., Pai, W.W., Chan, Y.H., Sun, W.L., Xu, C.Z., Lin, D.S., Chou, M.Y., Fedorov, A.V. and Chiang, T.C., "Large Quantum-Spin-Hall Gap in Single-Layer 1T′ WSe_2," *Nature Communications*, vol. 9, no. 1, pp. 1-7, 2018.

[19] Yang, G., Xu, Z., Liu, Z., Jin, S., Zhang, H. and Ding, Z., "Strain-and Fluorination-Induced Quantum Spin Hall Insulators in Blue Phosphorene: A First-Principles Study," *The Journal of Physical Chemistry C*, vol. 121, no. 23, pp. 12945-12952, 2017.

[20] He, X. and Li, J.B., "Hydrogenated Antimonene as Quantum Spin Hall Insulator: A First-Principles Study," *Chinese Physics B*, vol. 28, no. 3, p. 037301, 2019.

[21] Zhao, M., Zhang, X. and Li, L., "Strain-Driven Band Inversion and Topological Aspects in Antimonene," *Scientific Reports*, vol. 5, p. 16108, 2015.

[22] Wang, Y.P., Zhang, C.W., Ji, W.X., Zhang, R.W., Li, P., Wang, P.J., Ren, M.J., Chen, X.L. and Yuan, M., "Tunable Quantum Spin Hall Effect via Strain in Two-Dimensional

Arsenene Monolayer," *Journal of Physics D: Applied Physics*, vol. 49, no. 5, p. 055305, 2016.

[23] Zhao, J., Li, Y. and Ma, J., "Quantum Spin Hall Insulators in Functionalized Arsenene (AsX, X= F, OH and CH_3) Monolayers with Pronounced Light Absorption," *Nanoscale*, vol. 8, no. 18, pp. 9657-9666, 2016.

[24] Zhang, H., Ma, Y. and Chen, Z., "Quantum Spin Hall Insulators in Strain-Modified Arsenene," *Nanoscale*, vol. 7, no. 45, pp. 19152-19159, 2015.

[25] Reis, F., Li, G., Dudy, L., Bauernfeind, M., Glass, S., Hanke, W., Thomale, R., Schäfer, J. and Claessen, R., "Bismuthene on a SiC Substrate: A Candidate For a High-Temperature Quantum Spin Hall Material," *Science*, vol. 357, no. 6348, pp. 287-290, 2017.

[26] Wang, A., Du, A. and Zhao, M., "Prediction of a Large-Gap Quantum-Spin-Hall Insulator: Diamond-Like GaBi Bilayer," *Nano Research*, vol. 8, no. 12, pp. 3823-3829, 2015.

[27] Li, X., Dai, Y., Ma, Y., Wei, W., Yu, L. and Huang, B., "Prediction of Large-Gap Quantum Spin Hall Insulator and Rashba-Dresselhaus Effect in Two-Dimensional g-TlA (A= N, P, As, and Sb) Monolayer Films," *Nano Research*, vol. 8, no. 9, pp. 2954-2962, 2015.

[28] Zhang, R.W., Zhang, C.W., Ji, W.X., Li, S.S., Yan, S.S., Li, P. and Wang, P.J., "Functionalized Thallium Antimony Films as Excellent Candidates for Large-Gap Quantum Spin Hall Insulator," *Scientific Reports*, vol. 6, p. 21351, 2016.

[29] Padilha, J.E., Janotti, A., Fazzio, A. and da Silva, A.J.R., "Substrate-Supported Large-Band-gap Quantum Spin Hall Insulator Based on III-V Bismuth Layers. *Physical Review B*, vol. 94, no. 19, p. 195424, 2016.

[30] Gruznev, D.V., Eremeev, S.V., Bondarenko, L.V., Tupchaya, A.Y., Yakovlev, A.A., Mihalyuk, A.N., Chou, J.P., Zotov, A.V. and Saranin, A.A., " Two-Dimensional In–Sb Compound on Silicon as a Quantum Spin Hall Insulator," *Nano Letters*, vol. 18, no. 7, pp. 4338-4345, 2018.

[31] Yao, Y., et al., "Spin-orbit Gap of Graphene: First-Principles Calculations," *Physical Review B*, vol. 75, no. 5, p. 041401, 2007.

[32] Matthes, L., O. Pulci, and F. Bechstedt, "Massive Dirac Quasiparticles in the Optical Absorbance of Graphene, Silicene, Germanene, and Tinene," *Journal of Physics: Condensed Matter*, vol. 25, no. 39, p. 395305, 2013.

[33] Wang, Y.-p., et al., "Two-Dimensional Arsenene Oxide: A Realistic Large-Gap Quantum Spin Hall Insulator," *Applied Physics Letters*, vol. 110, no. 21, p. 213101, 2017.

[34] Zhang, S.-j., et al., "Intrinsic Dirac Half-Metal and Quantum Anomalous Hall Phase in a Hexagonal Metal-Oxide Lattice," *Physical Review B*, vol. 96, no. 20, p. 205433, 2017.

[35] Yu, W., et al., "Strain Induced Quantum Spin Hall Insulator in Monolayer β-BiSb from First-Principles Study," *RSC Advances*, vol. 7, no. 44, pp. 27816-27822, 2017.

[36] Balendhran, S., et al., "Elemental Analogues of Graphene: Silicene, Germanene, Stanene, and Phosphorene," *Small*, vol. 11, no. 6, pp. 640-652, 2015.

[37] Butler, S.Z., et al., "Progress, Challenges, and Opportunities in Two-Dimensional Materials Beyond Graphene," *ACS Nano*, vol. 7, no. 4, pp. 2898-2926, 2013.

[38] Yu, X.-L. and J. Wu, "Evolution of the Topological Properties of Two-Dimensional Group IVA Materials and Device Design," *Physical Chemistry Chemical Physics*, vol. 20, no. 4, pp. 2296-2307, 2018.

[39] Zhang, M.-h., et al., "Prediction of High-Temperature Chern Insulator with Half-Metallic Edge States in Asymmetry-Functionalized Stanene," *Nanoscale*, vol. 10, no. 43, pp. 20226-20233, 2018.

[40] Jia, Y.-z., et al., "Films Based on Group IV–V–VI Elements for the Design of a Large-Gap Quantum Spin Hall Insulator with Tunable Rashba Splitting," *RSC Advances*, vol. 7, no. 19, pp. 11636-11643, 2017.

[41] Liu, C.-C., W. Feng, and Y. Yao, "Quantum Spin Hall Effect in Silicene and Two-Dimensional Germanium," *Physical Review Letters*, vol. 107, no. 7, p. 076802, 2011.

[42] Liu, C.-C., H. Jiang, and Y. Yao, "Low-Energy Effective Hamiltonian Involving Spin-Orbit Coupling in Silicene and Two-Dimensional Germanium and Tin," *Physical Review B*, vol. 84, no. 19, p. 195430, 2011.

[43] Zhao, H., et al., "Unexpected Giant-Gap Quantum Spin Hall Insulator in Chemically Decorated Plumbene Monolayer," *Scientific Reports*, vol. 6, p. 20152, 2016.

[44] Lu, Y., et al., "Topological Properties of Atomic Lead Film with Honeycomb Structure," *Scientific Reports*, vol. 6, p. 21723, 2016.

[45] Xu, Y., et al., "Large-Gap Quantum Spin Hall Insulators in Tin Films," *Physical review letters*, vol. 111, no. 13, p. 136804, 2013.

[46] Zhang, R.-w., et al., "New Family of Room Temperature Quantum Spin Hall Insulators in Two-Dimensional Germanene Films," *Journal of Materials Chemistry C*, vol. 4, no. 10, pp. 2088-2094, 2016.

[47] Krawiec, M., "Functionalization of Group-14 Two-Dimensional Materials," *Journal of Physics: Condensed Matter*, vol. 20, no. 23, p. 233003, 2018.

[48] Zhao, H., et al., "First-Principles Prediction of a Giant-Gap Quantum Spin Hall Insulator in Pb Thin Film," *Physical Chemistry Chemical Physics*, vol. 18, no. 46, pp. 31862-31868, 2016.

[49] Ni, Z., et al., "Tunable Bandgap in Silicene and Germanene," *Nano letters*, vol. 11, no. 1, pp. 113-118, 2011.

[50] Nigam, S., et al., "Modulation of Bandgap by an Applied Electric Field in Silicene-Based Hetero-bilayers," *Physical Chemistry Chemical Physics*, vol. 17, no. 17, pp. 11324-11328, 2015.

[51] Gao, N., J. Li, and Q. Jiang, "Bandgap Opening in Silicene: Effect of Substrates," *Chemical Physics Letters*, vol. 592, pp. 222-226, 2014.

[52] Yan, W.-W., et al., "Family-Dependent Magnetism in Atomic Boron Adsorbed Armchair Graphene Nanoribbons," *Journal of Materials Chemistry C*, vol. 7, no. 21, pp. 6241-6245, 2019.

[53] Sahin, H. and F.M. Peeters, "Adsorption of Alkali, Alkaline-Earth, and 3d Transition Metal Atoms on Silicene," *Physical Review B*, vol. 87, no. 8, p. 085423, 2013.

[54] Ezawa, M., "A Topological Insulator and Helical Zero Mode in Silicene Under an Inhomogeneous Electric Field," *New Journal of Physics*, vo. 14, no. 3, p. 033003, 2012.

[55] Padilha, J., et al., "A New Class of Large Bandgap Quantum Spin Hall Insulators: 2D Fluorinated Group-IV binary compounds," *Scientific Reports*, vol. 6, p. 26123, 2016.

[56] Wu, J., et al., "Controlled Chlorine Plasma Reaction for Noninvasive Graphene Doping," *Journal of the American Chemical Society*, vol. 133, no. 49, pp. 19668-19671, 2011.

[57] Kim, K.N., V.P. Pham, and G.Y. Yeom, "Chlorine Radical Doping of a Few Layer Graphene with Low Damage," *ECS Journal of Solid State Science and Technology*, vol. 4, no. 6, pp. N5095-N5097, 2015.

[58] Wu, L., K. Gu, and Q. Li, "New Families of Large Bandgap 2D Topological Insulators in Ethynyl-Derivative Functionalized Compounds," *Applied Surface Science*, vol. 484, pp. 1208-1213, 2019.

[59] Zhang, R.-W., et al., "Ethynyl-Functionalized Stanene Film: A Promising Candidate as Large-gap Quantum Spin Hall Insulator," *New Journal of Physics*, vol. 17, no. 8, p. 083036, 2015.

[60] Li, S.-s., et al., "Robust Room-Temperature Quantum Spin Hall Effect in Methyl-Functionalized InBi Honeycomb Film," *Scientific Reports*, vol. 6, p. 23242, 2016.

[61] Ma, Y., et al., "Strain-Induced Quantum Spin Hall Effect in Methyl-Substituted Germanane GeCH3," *Scientific Reports*, vol. 4, p. 7297, 2014.

[62] Ren, C.-C., et al., "Strain-Induced Quantum Spin Hall Effect in Two-Dimensional Methyl-Functionalized Silicene $SiCH_3$," *Nanomaterials*, vol. 8, no. 9, p. 698, 2018.

[63] Upadhyaya, P. and Tserkovnyak, Y., "Domain Wall in a Quantum Anomalous Hall Insulator as a Magnetoelectric Piston," *Physical Review B*, vol. 94, no. 2, pp. 020411, 2016.

[64] Upadhyaya, P., Kim, S.K. and Tserkovnyak, Y., "Magnetic Domain Wall Floating on a Spin Superfluid," *Physical Review Letters*, vol. 118, no. 9, pp. 097201, 2017.

[65] Johnson, M.B., Johnson and Mark B., "Magnetic Spin Transistor Hybrid Circuit Element", *U.S. Patent* 5,565 695, 1996.

[66] Hsu, S.T., Tang, J. and Sakiyama, K., Sharp Laboratories of America Inc, "Spin Transistor Magnetic Random Access Memory Device" U.S. Patent 6,753,562, 2004.

[67] Grollier, J., Querlioz, D. and Stiles, M.D., "*Spintronic Nanodevices for Bioinspired Computing*", Proceedings of the IEEE, vol. 104, no. 10, pp.2024-2039, 2016.

[68] Kang, W., Zhang, Y., Wang, Z., Klein, J.O., Chappert, C., Ravelosona, D., Wang, G., Zhang, Y. and Zhao, W., "*Spintronics: Emerging Ultra-Low-Power Circuits and Systems Beyond MOS Technology*", ACM Journal on Emerging Technologies in Computing Systems (JETC), vol. 12, no. 2, pp. 1-42, 2015.

[69] Makarov, A., Windbacher, T., Sverdlov, V. and Selberherr, S., "*CMOS-Compatible Spintronic Devices: A Review*", Semiconductor Science and Technology, vol. 31, no. 11, pp. 113006, 2016.

[70] Bandyopadhyay, S. and Cahay, M., "Introduction to Spintronics", CRC Press, 2015.

[71] Hellman, F., Hoffmann, A., Tserkovnyak, Y., Beach, G.S., Fullerton, E.E., Leighton, C., MacDonald, A.H., Ralph, D.C., Arena, D.A., Dürr, H.A., and Fischer, P., "Interface-Induced Phenomena in Magnetism," *Reviews of Modern Physics*, vol. 89, no. 2, pp. 025006, 2017.

[72] Dreizler, R.M. and Gross, E.K., "Density Functional Theory: An Approach to the Quantum Many-Body Problem", *Springer Science and Business Media*, 2012.

[73] Burke, K., "Perspective on Density Functional Theory", *The Journal of chemical physics*, vol. 136, no. (15), pp. 150901, 2012.

[74] Xia, Y., Qian, D., Hsieh, D., Wray, L., Pal, A., Lin, H., Bansil, A., Grauer, D., Hor, Y. S., Cava, R. J., Hasan, M. Zahid, "Discovery (Theoretical Prediction and Experimental Observation) of a Large-Gap Topological-Insulator Class with Spin-Polarized Single-Dirac-Cone on the Surface", *Nature Physics*, vol. 5, pp. 398-402, 2009.

[75] Hsieh, D., Xia, Y., Wray, L., Qian, D., Pal, A., Dil, J.H., Osterwalder, J., Meier, F., Bihlmayer, G., Kane, C.L. and Hor, Y.S., "Observation of Unconventional Quantum Spin Textures in Topological Insulators", *Science*, vol. *323, no.* 5916, pp. 919-922, 2009.

[76] Hsieh, D., Qian, D., Wray, L., Xia, Y., Hor, Y.S., Cava, R.J. and Hasan, M.Z., "A Topological Dirac Insulator in a Quantum Spin Hall Phase", *Nature*, vol. 452, no. 7190, pp. 970-974, 2008.

[77] Zhang, S.C., "Topological States of Quantum Matter", *Physics*, vol. *1*, p.6, 2008.

[78] Version, A.T., Synopsys QuantumWise A/S. S.[(accessed on 25 September 2018)], 2017.

[79] Hohenberg, P., and Kohn, W., "Inhomogenous Electron Gas", *Physical Review*, vol. 136, no. 3B, pp. 864-871, 1964.

[80] Kohn, W., and Sham, L. J., "Self-Consistent Equations Including Exchange and Correlation Effects", *Physical Review*, vol. 140, no. 4A, pp. A1133-A1138, 1965.

[81] Negele, J.W., “Structure of Finite Nuclei in the Local-Density Approximation”, *Physical Review C*, vol. 1, no. 4, pp. 1260, 1970.

[82] Perdew, J.P., Burke, K. and Ernzerhof, M., “Generalized Gradient Approximation Made Simple”, *Physical Review Letters*, vol. *77, no.* 18, pp. 3865, 1996.

[83] Pickett, W.E., “Pseudopotential Methods in Condensed Matter Applications”, *Computer Physics Reports*, vol. 9, no. 3, pp. 115-197, 1989.

[84] Byrd, R.H., et al., "A Limited Memory Algorithm for Bound Constrained Optimization," *SIAM Journal on Scientific Computing*, vol. 16, no. 5, pp. 1190-1208, 1995.

[85] Perdew, J.P., K. Burke, and M. Ernzerhof, "Generalized Gradient Approximation Made Simple," *Physical Review Letters*, vol. 77, no. 18, p. 3865, 1996.

[86] Monkhorst, H.J. and J.D. Pack, "Special Points for Brillouin-Zone Integrations," *Physical Review B*, vol. 13, no. 12, p. 5188, 1976.

[87] Stokbro, K., B.K. Nikolic, and A.M. Bratkovsky, "Computing Noncollinear Spins and Spin Torque in ATK from QuantumWise A/S," 2013.

[88] Garrity, K.F., et al., "Pseudopotentials for High-Throughput DFT Calculations," *Computational Materials Science*, vol. 81, pp. 446-452, 2014.

[89] Xiao, H., Tahir-Kheli, J. and Goddard III, W.A., “Accurate Band Gaps for Semiconductors from Density Functional Theory”, *The Journal of Physical Chemistry Letters*, vol. 2, no. 3, pp. 212-217, 2011.

[90] Zhu, F.F., Chen, W.J., Xu, Y., Gao, C.L., Guan, D.D., Liu, C.H., Qian, D., Zhang, S.C. and Jia, J.F., “Epitaxial Growth of Two-Dimensional Stanene”, *Nature materials*, vol. 14, no. 10, pp.1020-1025, 2015.

[91] Yang, W., Chen, G., Shi, Z., Liu, C.C., Zhang, L., Xie, G., Cheng, M., Wang, D., Yang, R., Shi, D. and Watanabe, K., “Epitaxial Growth of Single-Domain Graphene on Hexagonal Boron Nitride”, *Nature materials*, vol. 12, no. 9, pp.792-797, 2013.

[92] Garcia, J. C., De Lima, D. B., Assali, L. V., and Justo, J. F., “Group IV Graphene and Graphane Like Nanosheets”, *The Journal of Physical Chemistry C*, vol. 115, no. 27, pp. 13242-13246, 2011.

[93] Libit, L. and Hoffmann, R., "Detailed Orbital Theory of Substituent Effects. Charge Transfer, Polarization, and the Methyl Group", *Journal of the American Chemical Society*, vol. 96, no. 5, pp.1370-1383, 1974.

[94] Fu, Liang; Kane, C. L., "Topological Insulators with Inversion Symmetry," Physical Review B, vol. 76, no. 4, pp. 045302, 2007.

[95] Zaveh, S.J., Roknabadi, M.R., Morshedloo, T. and Modarresi, M., "Electronic and Thermal Properties of Germanene and Stanene by First-Principles Calculations", *Superlattices and Microstructures*, vol. *91*, pp. 383-390, 2016.

[96] Bandyopadhyay, S. and Cahay, M., "Introduction to Spintronics", *CRC Press*, 2015.

[97] Griffiths, D.J. and Schroeter, D.F., "*Introduction to quantum mechanics*", Cambridge University Press, 2018.

[98] Hall, E. H., "On a New Action of the Magnet on Electric Currents", *American Journal of Mathematics*, vol. 2, no. 3, pp. 287-292, 1879.

[99] Kellogg, M., Eisenstein, J., Pfeiffer, L.N. and West, K.W., "*Vanishing Hall Resistance at High Magnetic Field in a Double-Layer Two-Dimensional Electron System*", Physical Review Letters, vol. 93, no. 3, pp. 036801-1-036801-4, 2004.

[100] Casas, O.E., Arrachea, L., Herrera, W.J. and Yeyati, A.L., "*Proximity Induced Time-Reversal Topological Superconductivity in Bi_2Se_3 Films Without Phase Tuning*", Physical Review B, vol. 99, no. 16, pp. 161301-1-161301-9, 2019.

[101] Bonderson, P., Nayak, C. and Qi, X.L., "A Time-Reversal Invariant Topological Phase at the Surface of a 3D Topological Insulator", *Journal of Statistical Mechanics: Theory and Experiment*, vol. 09, pp. 09016-1-09016-18, 2013.

[102] Okada, Y., Dhital, C., Zhou, W., Huemiller, E.D., Lin, H., Basak, S., Bansil, A., Huang, Y.B., Ding, H., Wang, Z. and Wilson, S.D., "*Direct Observation of Broken Time-Reversal Symmetry on the Surface of a Magnetically Doped Topological Insulator*", Physical Review Letters, vol. 106, no. 20, pp. 206805, 2011.

[103] Eschrig, H. and Richter, M., "Kramers' Theorem in the Relativistic Electronic Structure Calculation", *Solid State Communications*, vol. 59, no. 12, pp. 861-864, 1986.